# APPLICATION OF THE QUANTAL DIFFUSION APPROACH BASED ON THE STOCHASTIC MEAN-FIELD THEORY

A THESIS SUBMITTED TO
THE GRADUATE SCHOOL OF NATURAL AND APPLIED SCIENCES
OF
MIDDLE EAST TECHNICAL UNIVERSITY

BY

ARDA KAYAALP

IN PARTIAL FULFILLMENT OF THE REQUIREMENTS
FOR
THE DEGREE OF MASTER OF SCIENCE
IN
PHYSICS

AUGUST 2024

Approval of the thesis:

**APPLICATION OF THE QUANTAL DIFFUSION APPROACH BASED ON THE STOCHASTIC MEAN-FIELD THEORY**

submitted by **ARDA KAYAALP** in partial fulfillment of the requirements for the degree of **Master of Science in Physics Department, Middle East Technical University** by,

Prof. Dr. Naci Emre Altun
Dean, Graduate School of **Natural and Applied Sciences** _____

Prof. Dr. Seçkin Kürkcüoğlu
Head of Department, **Physics** _____

Prof. Dr. Osman Yılmaz
Supervisor, **Department of Physics, METU** _____

Prof. Dr. Şakir Ayık
Co-supervisor, **Physics Dept., Tennessee Tech University** _____

**Examining Committee Members:**

Prof. Dr. İsmail Turan
Department of Physics, METU _____

Prof. Dr. Osman Yılmaz
Department of Physics, METU _____

Prof. Dr. Tahmasib Aliyev
Department of Physics, METU _____

Prof. Dr. Gürsevil Turan
Department of Physics, METU _____

Prof. Dr. Bülent Yılmaz
Department of Physics, Ankara University _____

Date: 06.08.2024

**I hereby declare that all information in this document has been obtained and presented in accordance with academic rules and ethical conduct. I also declare that, as required by these rules and conduct, I have fully cited and referenced all material and results that are not original to this work.**

Name, Surname: Arda Kayaalp

Signature :

# ABSTRACT

## APPLICATION OF THE QUANTAL DIFFUSION APPROACH BASED ON THE STOCHASTIC MEAN-FIELD THEORY

Kayaalp, Arda
M.S., Department of Physics
Supervisor: Prof. Dr. Osman Yılmaz
Co-Supervisor: Prof. Dr. Şakir Ayık

August 2024, 75 pages

This thesis investigates the application of the quantal diffusion approach based on Stochastic Mean-Field (SMF) theory to low-energy heavy-ion collisions, with a focus on multinucleon transfer (MNT) reactions. The study specifically examines the reactions of $^{58}$Fe + $^{208}$Pb at $E_{\text{c.m.}} = 238.5$ MeV, $^{36}$S + $^{238}$U at $E_{\text{c.m.}} = 151.1$ MeV, $^{64}$Ni + $^{130}$Te at $E_{\text{c.m.}} = 184.3$ MeV, and $^{206}$Pb + $^{118}$Sn at $E_{\text{c.m.}} = 436.8$ MeV. The Time-Dependent Hartree-Fock (TDHF) theory, widely utilized for analyzing reaction dynamics, is extended by incorporating SMF theory to address the limitations related to fluctuations and deviations in fragment mass and charge distributions. This approach allows for a more accurate description of the complex dynamics involved in MNT processes. Primary production yields and secondary cross-sections are thoroughly analysed after evaporation and calculated using the statistical de-excitation model with the GEMINI++ toolkit. The results demonstrate a good agreement with experimental data, validating the effectiveness of the SMF approach. This integration of SMF and GEMINI++ significantly enhances the precision of predicting reaction outcomes, contributing to a deeper understanding of nuclear reaction mechanisms.

Keywords: Stochastic Mean-Field Theory, Time-Dependent Hartree-Fock Theory, Multi-Nucleon Transfer Mechanism, Low Energy Heavy-Ion Reactions

# ÖZ

## STOKASTİK ORTALAMA ALAN TEORİSİNE DAYALI KUANTAL DİFÜZYON YAKLAŞIMININ UYGULAMASI

Kayaalp, Arda
Yüksek Lisans, Fizik Bölümü
Tez Yöneticisi: Prof. Dr. Osman Yılmaz
Ortak Tez Yöneticisi: Prof. Dr. Şakir Ayık

Ağustos 2024 , 75 sayfa

Bu tez, düşük enerjili ağır iyon çarpışmalarına Stokastik Ortalama Alan (SOA) teorisine dayalı kuantal difüzyon yaklaşımının uygulanmasını, çoklu nükleon transfer (MNT) reaksiyonları çerçevesinde araştırmaktadır. Çalışma $^{58}$Fe + $^{208}$Pb reaksiyonunu $E_{\text{c.m.}} = 238.5$ MeV enerji seviyesinde, $^{36}$S + $^{238}$U reaksiyonunu $E_{\text{c.m.}} = 151.1$ MeV enerji seviyesinde, $^{64}$Ni + $^{130}$Te reaksiyonunu $E_{\text{c.m.}} = 184.3$ MeV enerji seviyesinde ve $^{206}$Pb + $^{118}$Sn reaksiyonunu $E_{\text{c.m.}} = 436.8$ MeV enerji seviyesinde incelemektedir. Reaksiyon dinamiklerini analiz etmek için yaygın olarak kullanılan Zamana Bağımlı Hartree-Fock teorisi (TDHF), çarpışma sonrası ortaya çıkan ürünlerin kütle ve yük dağılımlarındaki dalgalanma ve sapmalara ilişkin sınırlamaları ele almak için SOA teorisini içererek genişletilmiştir. Bu yaklaşım, MNT süreçlerinde yer alan karmaşık dinamiklerin daha doğru bir şekilde tanımlanmasına olanak tanır. Birincil ürünlerin üretim dağılımları ve GEMINI++ kodu ile hesaplanan istatistiksel soğuma modeli kullanılarak buharlaşma sonrası ortaya çıkan ikincil ürünlerin tesir kesitleri analiz edilmiştir. Sonuçlar, deneysel verilerle iyi bir uyum göstererek SMF yakla-

şımının etkinliğini doğrulamaktadır. SOA ve GEMINI++ kütüphanesinin bu entegrasyonu, reaksiyon sonuçlarının tahmin edilmesinin doğruluğunu önemli ölçüde artırarak, düşük-enerjili ağır-iyonları içeren nükleer reaksiyon mekanizmalarının daha derinlemesine anlaşılmasına katkıda bulunmaktadır.

Anahtar Kelimeler: Stokastik Ortalama Alan Kuramı, Zamana Bağlı Hartree-Fock Kuramı, Çoklu Nükleon Transfer Mekanizması, Düşük Enerjili Ağır İyon Reaksiyonları

*To my mother, who always encouraged me to follow my dreams,*
*to my father, who ignited my love for physics.*

## ACKNOWLEDGMENTS

The graduate experience is profoundly influenced by the academic advisor. I was fortunate to work with Prof. Dr. Osman Yılmaz during my master's studies. His invaluable support and guidance in both academic and personal matters enabled me to navigate my studies more comfortably and confidently. For his unwavering assistance, I will always be deeply grateful.

I would like to extend my deepest thanks to my co-advisor, Prof. Dr. Şakir Ayık, for many illuminating and fruitful discussions on the theory. I also want to express my gratitude to Prof. Dr. A. Sait Umar for his assistance with computational methodologies.

I am grateful to my examining committee members, Prof. Dr. İsmail Turan, Prof. Dr. Tahmasib Aliyev, Prof. Dr. Gürsevil Turan, and Prof. Dr. Bülent Yılmaz, for taking their valuable time to review this work and providing their thoughtful feedback.

I would like to express my heartfelt gratitude to my dearest Deniz Özmen for her unwavering support during these times.

I am immeasurably grateful to my beloved family. To my brother, for his constant support. To my father, who tirelessly works to pour all his resources into allowing us to chase our dreams. And to my sweet mother, who, despite fighting her own battles, never stopped shining her bright light upon us. For their love and support, I will forever be thankful.

Finally, I would like to thank the Scientific and Technological Research Council of Turkey (TUBITAK) for their financial support through the 2210-A General Domestic Master's Scholarship Program. I also extend my gratitude to TUBITAK ULAKBIM, High Performance and Grid Computing Center (TRUBA resources), where all the numerical calculations presented in this work were conducted. I acknowledge that this project is partially supported by the TUBITAK with Grant No. 122F150.

## TABLE OF CONTENTS

## LIST OF TABLES

TABLES

## LIST OF FIGURES

FIGURES

## LIST OF ABBREVIATIONS

| | |
|---|---|
| CM | Center-of-Mass |
| CN | Compound Nucleus |
| DIC | Deep-Inelastic Collision |
| EDF | Energy Density Functional |
| FF | Fusion-Fission |
| MNT | Multi-Nucleon Transfer |
| QF | Quasi-Fission |
| SHE | Super-Heavy Element |
| SMF | Stochastic Mean-Field |
| TDHF | Time-Dependent Hartree-Fock |
| TDRPA | Time-Dependent Random Phase Approximation |
| TKE | Total Kinetic Energy |

# CHAPTER 1

# INTRODUCTION

## 1.1 A Brief Description of the Atomic Nuclei

An atom's mass comes mainly from its tiny, dense nucleus at the center of the atomic complex and measures about $\approx 10^{-14}$ meters across. The nucleus comprises protons and neutrons, collectively known as nucleons, and is identified by the neutron number $N$ and the proton number $Z$. A unique combination of these numbers forms a nuclide, symbolically represented as ${}^{A}_{Z}X_{N}$, where $A$ is the mass number ($A = N + Z$), and $X$ is the element symbol corresponding to the atomic number $Z$. Nuclei with the same number of protons but different numbers of neutrons are called isotopes. Those with the same number of neutrons but different numbers of protons are known as isotones. Nuclei that share the same mass number are referred to as isobars.

The atomic nucleus is a finite, self-bound, non-relativistic quantum many-body system of protons and neutrons [1]. These two kinds of fermions interact through the nuclear force. The nucleus is self-bound because of attractive nuclear interactions and has no internal core like an atomic system. The range of the nuclear force is finite; the distance between nucleons is represented by $d$, and the attractive component of the force extends to around $d \approx 1.4$ femtometers (fm), while the repulsive component occurs at distances less than $d \approx 0.5$ fm.

The primary focus of our research is the study of nuclear reactions, which serve as illustrations of quantum many-body dynamics. Our primary objective is to utilize a microscopic quantum many-body theory to accurately predict the optimal processes for generating specific nuclei. These theoretical projections have the potential to enable the examination of unstable nuclei that have not yet been synthesized.

Multi-nucleon transfer (MNT) and quasi-fission (QF) events in low-energy heavy-ion reactions are examples of non-equilibrium quantum many-body dynamics. They have gained great attention because they provide insights into the microscopic reaction mechanisms that reveal both colliding nuclei's static and dynamic features. These procedures have recently gained attention as potentially effective ways to produce unstable nuclei that are challenging to produce in other ways [2].

The transfer of many nucleons between two colliding nuclei occurs in both MNT and QF processes. You could think of QF processes as a specific type of MNT. Several variables affect the dynamics of these transfers, such as the projectile and target combination, the incident energy, the initial angular momenta, and the relative orientations if the colliding partners have ground state deformations.

### 1.2 Heavy-Ion Reactions and Means to Produce Super-Heavy Elements (SHE)

A nuclear reaction occurs when ions approach closely enough to interact via the nuclear force, leading to structural changes in their atomic nuclei. Nuclear reactions are classified as low-energy heavy-ion reactions if the interacting ions are larger than helium nuclei and the bombardment energy per nucleon is roughly $\approx 10$ MeV per nucleon. The impact parameter ($b$), or the initial orbital angular momentum ($\ell$), defines the closeness to the central collision in low-energy heavy-ion collisions. The impact parameter is the perpendicular distance measured from the center of the projectile nuclei to the central beam axis, shown as a dashed line in Fig. 1.1. In terms of the impact parameter ($b$), the initial angular momentum ($\ell$) can be also defined as,

$$\ell = b(2\mu E_{c.m.})^{1/2}, \tag{1.1}$$

where $\mu$ is the reduced mass of the reaction system. When the impact parameter exceeds the combined radii of the two atomic nuclei, referred to as distant collisions, the ions do not come close enough for significant nuclear interaction. In this case, only the Coulomb force affects their trajectory, leading to elastic and quasi-elastic reactions. Nuclear interaction becomes more significant as the impact parameter decreases to the grazing impact parameter, equal to the sum of the radii of the two nuclei.

This leads to multiple nucleon exchanges between the colliding ions, known as grazing collisions. Some of the bombardment energy dissipates into internal degrees of freedom, heating the system. The two-center nuclear system may rotate together for a while before separating, a phenomenon known as deep-inelastic collisions (DIC).

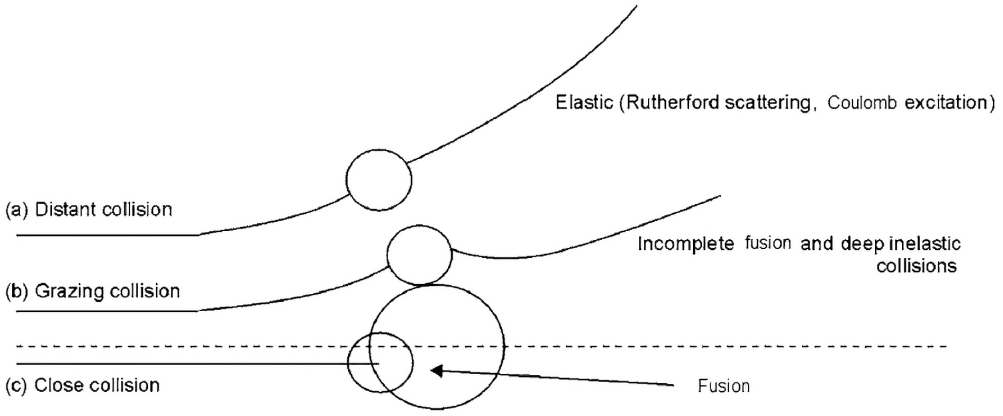


Figure 1.1: Classical trajectories of heavy-ion collisions [3].

As the impact parameter decreases further, the nuclei interact very strongly, classified as close collisions. In close collisions involving relatively light systems, the projectile and target nuclei may fuse to form a hot compound nucleus, a process known as nuclear fusion.

Elements heavier than plutonium (atomic number $Z = 94$) are unstable and do not occur naturally; they are produced artificially through nuclear reactions and elements with atomic numbers $Z \geq 104$ are called superheavy elements and are produced via fusion reactions of heavy nuclei. The production cross-section in these reactions is very small (around a few picobarns), making it crucial to understand the reaction mechanisms theoretically. Various factors such as collision energy, mass symmetry, deformation, isospin, and the shell structure of the colliding nuclei affect the fusion probability. Isolating the effect of a single variable is a challenging task to achieve.

Fusion reactions occur in three stages. In the first stage, the projectile nucleus overcomes the Coulomb barrier and fuses with the target nucleus. The fused system reaches thermal equilibrium in the second stage, forming a hot compound nucleus. In the third stage, the excited compound nucleus cools down by splitting into smaller

nuclei, fusion-fission (FF), or emitting light particles like neutrons, protons, and alpha particles, a process known as fusion-evaporation. Superheavy elements are produced as fusion products through the evaporation residue at the end of this cooling process.

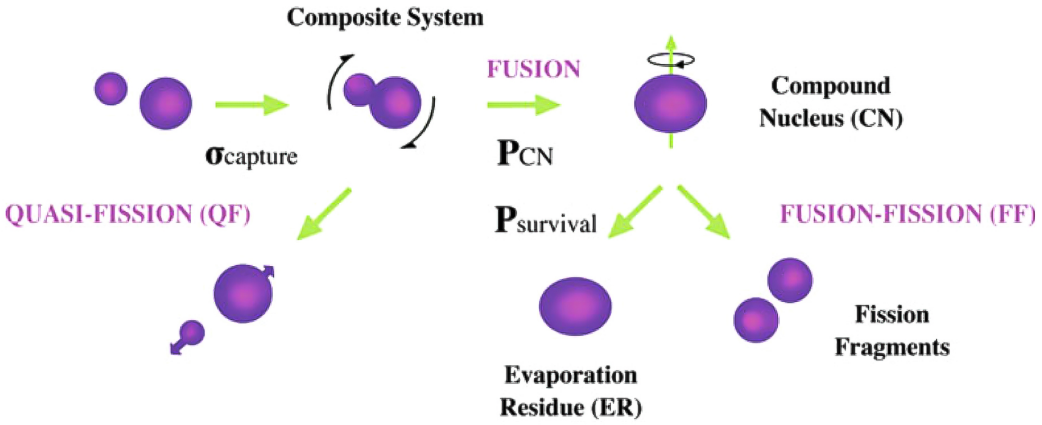


Figure 1.2: A schematic representation of a heavy-ion collision around the Coulomb barrier [4].

In heavy systems, the reaction mechanism develops differently from the fusion process, as shown in Fig. 1.2. Specifically, in systems where the Coulomb factor calculated as the product of charge numbers exceeds a critical value ($Z_1 Z_2 > 1600$), the projectile and target nuclei stick together during the collision, forming a two-center structure similar to deep-inelastic reactions. Multiple nucleons are exchanged through the hypothetical window between the two nuclei, maintaining the total mass number. At the same time, a significant portion of the bombardment energy and angular momentum transfers into internal degrees of freedom. Without forming a compound nucleus, the system may separate into two nuclei with different proton and neutron numbers from the initial values. This mechanism, which prevents the formation of a compound nucleus, is known as QF. These reactions in heavy systems represent an intermediate reaction mechanism between DIC and the fusion reaction of a compound nucleus. Understanding this mechanism is important for MNT processes and synthesising super-heavy elements (SHE). Additionally, QF reactions provide a suitable method for obtaining heavy nuclei rich in neutrons and protons. The MNT mechanism observed in these reactions may enable the creation of transuranium-heavy elements. Studying new elements and the static and dynamic properties of unstable

nuclei rich in protons and neutrons, particularly those near the nucleon drip line, are currently significant and current research topics in heavy-ion physics [5, 6].

Fusion-evaporation reactions around the Coulomb barrier energies are the only way to produce SHE. However, the formation of SHE after evaporation is hindered by FF and QF processes, which are the two effective reactions preventing the formation of a compound nucleus (CN) through fusion, following different paths during the CN formation and having different average contact times. The typical contact time for QF is about $10^{-20}$ seconds, whereas, for FF reactions, it is about $10^{-16}$ seconds [7, 8]. Consequently, QF is the primary reaction mechanism that hinders the formation of super-heavy nuclei. Additionally, while the FF process exhibits significant mass transfer, QF processes show minimal mass transfer related to their contact time.

It is important to develop theoretical models to analyze experimental data and select appropriate projectile and target nuclei for the intended purpose. Various macroscopic transport models have been proposed to explain the evolution of collective variables in deep-inelastic heavy-ion collisions and QF reactions. In these models, the system's potential energy and transport coefficients are empirically calculated [9].

### 1.3 Outline of The Thesis

In this work, we employed a quantal diffusion description of multi-nucleon transfer in heavy-ion collisions based on the stochastic mean-field (SMF) approach, offering a fully microscopic description without adjustable parameters. The thesis is structured into five chapters. Chapter 1 introduces the problem and the motivation. Chapter 2 delves into the time-dependent Hartree-Fock theory (TDHF) and its application to selected heavy-ion reaction systems, establishing the foundation for subsequent chapters. Chapter 3 extends this description stochastically using the SMF approach, incorporating fluctuations and correlations into the TDHF model. Chapter 4 utilizes the results from the SMF approach to calculate production yields and cross-sections, comparing theoretical results with experimental data and analyzing differences. Chapter 5 summarizes the key findings, emphasizing the contributions of the quantal diffusion description and SMF approach to our understanding of multi-nucleon transfer

in heavy-ion collisions, and suggests directions for future research.

# CHAPTER 2

## TDHF THEORY AND ITS APPLICATION TO THE MNT REACTIONS

Characterizing nuclear events and determining their results is a substantial effort because of the multitude of potential reactions that can occur, frequently competing with one another at a specific collision energy. Mean-field theories, which involve the independent evolution of particles within a mean-field created by a group of particles, have emerged as fundamental microscopic approaches for characterizing nuclear dynamics. These techniques have undergone significant advancements in recent years [10].

Dirac established the theory of Time-Dependent Hartree-Fock (TDHF) in 1930 to explain the behaviour of electrons in atoms [11]. Research on nuclear collision dynamics started in the 1970s [12]. Most current TDHF computations employ three-dimensional models that incorporate comprehensive Skyrme functionals, which also account for time-odd components [13]. The Skyrme interactions are chosen to accurately replicate a wide range of nuclear properties across different mass nuclei without requiring individual parameter adjustments for each reaction. Overall, TDHF theory proved to be reliable in characterizing low-energy nuclear processes.

The TDHF theory is microscopic and gives a detailed account of nuclear dynamics. This capability is crucial for understanding the behaviour of nuclei during reactions. TDHF can describe many nuclear phenomena, such as heavy-ion fusion, fission, and MNT reactions. Once an energy density functional (EDF) is defined, TDHF needs no further empirical parameters. This property increases its predictive power and diminishes the dependence on experimental data for parameter tuning. One of the most critical limitations of TDHF is its mean-field approximation, which assumes that all particles move independently inside the average field this ensemble generates [14,

15]. Such an assumption may lead to neglecting critical two-body correlations, failing to describe some processes like multi-nucleon transfer and quantum tunneling [10]. The TDHF theory is semi-classical by construction and optimized to predict average quantities rather than the fluctuation or distribution of observables. Therefore, it often underestimates distributions of observables, implying a more detailed treatment is required under quantum mechanics. The single-determinant formalism of TDHF also tends to underestimate fluctuations and correlations of one-body observables. Beyond mean-field methods have been developed to manage these drawbacks, like the Time-Dependent Random Phase Approximation (TDRPA) and the SMF approach [9].

A brief description of the Hartree-Fock equations with Skyrme effective interactions will be provided in later sections of this chapter. Subsequently, we shall expand this framework into the time domain to better understand the dynamics of nuclear processes, leading to the formulation of the TDHF equations. Finally, we will present the results of TDHF calculations for $^{58}$Fe + $^{208}$Pb reaction with $E_{\text{c.m.}}$ = 238.5 MeV, $^{36}$S + $^{238}$U reaction with $E_{\text{c.m.}}$ = 151.1 MeV, $^{64}$Ni + $^{130}$Te reaction with $E_{\text{c.m.}}$ = 184.3 MeV and $^{206}$Pb + $^{118}$Sn reaction with $E_{\text{c.m.}}$ = 436.8 MeV, where $E_{\text{c.m.}}$ represents the initial collision energy of the reaction system in the center-of-mass frame.

## 2.1 Hartree-Fock Equations

According to the Hartree-Fock approach, one can investigate the structural properties of nuclei by treating each nucleon as moving independently within a mean field, which is an average potential. The interactions between each nucleon in the nucleus produce this mean-field. As with other fermions, nucleons are governed by the Pauli exclusion principle. The wave function of the collective state must be antisymmetric when two nucleon coordinates are exchanged. The Hartree-Fock approximation states that the trial wave function of a nucleus containing $A$ nucleons can be expressed as a Slater determinant, a product of antisymmetrized occupied states [16].

A Slater determinant is formed by using a set of single-particle wave functions, called the Hartree-Fock basis, $\phi_i(r_i)$, where $r_j$ represents the spatial, spin, and isospin coordinates of the $j$th nucleon. The construction of the Slater determinant follows this

definition,

$$\Phi\left(r_1 \ldots r_A\right) \rightarrow \Phi_{HF}\left(r_1 \ldots r_A\right) = \frac{1}{\sqrt{A!}} \begin{vmatrix} \phi_1\left(r_1\right) & \phi_1\left(r_2\right) & \cdots & \phi_1\left(r_A\right) \\ \phi_2\left(r_1\right) & \phi_2\left(r_2\right) & \cdots & \phi_2\left(r_A\right) \\ \vdots & \vdots & \ddots & \vdots \\ \phi_A\left(r_1\right) & \phi_A\left(r_2\right) & \cdots & \phi_A\left(r_A\right) \end{vmatrix} . \quad (2.1)$$

Although the precise shape of the individual particle wave functions within a nucleus is initially uncertain, they can be estimated using oscillator wave functions. This approximation is true when the number of wave functions corresponds to the number of nucleons in the nucleus unless pairing correlations are included. The initial step involves considering the complete many-body Hamiltonian, which may be represented in terms of a one-body kinetic energy term and a two-body force for a system consisting of $A$ particles, as stated below,

$$\hat{H} = \sum_{i=1}^{A} \frac{\hat{p}_i^2}{2m_i} + \frac{1}{2} \sum_{i \neq j}^{A} V\left(r_i, r_j\right). \quad (2.2)$$

In this instance, the nucleon-nucleon force, which includes the Coulomb interaction, is denoted by $V(r_i, r_j)$. The primary concept behind the mean-field technique is to represent the two-body potential, $V(r_i, r_j)$, by a one-body mean-field, $U(r_i)$, while incorporating as much of the physics as possible. The average value of the entire Hamiltonian for the Hartree-Fock wave function provides an approximation of the ground-state energy in the Hartree-Fock method.

$$\begin{aligned} E_{HF}^0 &= \left\langle \Phi_{HF} \left| \hat{H} \right| \Phi_{HF} \right\rangle \\ &= -\frac{\hbar^2}{2m} \sum_{i=1}^{A} \int \phi_i^*(r) \nabla^2 \phi_i(r)\, dr \\ &\quad + \frac{1}{2} \sum_{i \neq j}^{A} \iint \phi_i^*(r) \phi_j^*(r') V(r, r') \phi_i(r) \phi_j(r')\, dr\, dr' \\ &\quad - \frac{1}{2} \sum_{i \neq j}^{A} \iint \phi_i^*(r) \phi_j^*(r') V(r, r') \phi_i(r') \phi_j(r)\, dr\, dr'. \end{aligned} \quad (2.3)$$

Here, the integral $\int d\boldsymbol{r} = \sum_{\sigma,q} \int d^3r$ is employed. The final term in the previously mentioned expression accounts for the antisymmetrization of the wave function when exchanging any pair of particles. The optimal Slater determinant to describe the ground state of the system is the one that minimizes the expectation value of energy. Afterwards, the optimal arrangement is determined by applying the variational principle, which aims to minimize the expected energy value by considering all potential single-particle wave functions.

$$\frac{\delta}{\delta\phi_a^*(r)}\left(E_{HF}^0 - \sum_{i=1}^{A}\epsilon_i \int |\phi_i(r)|^2 \, dr\right) = 0, \tag{2.4}$$

in which,

$$\frac{\delta}{\delta\phi_a^*(r)}\left\{\phi_i^*(r')\right\} = \delta_{ia}\delta(r-r'). \tag{2.5}$$

The Lagrange multipliers, denoted as $\epsilon_i$ in Eq. 2.4, provide the function of assuring the proper normalizing of the wave functions and including the constraint that ensures the conservation of particle number inside the system as,

$$\sum_{i=1}^{A} \int |\phi_i(r)|^2 \, dr = A. \tag{2.6}$$

Now, substituting ground state EDF in Eq. 2.3 to the principle of least action defined as in Eq. 2.4, we obtain The Hartree-Fock equations as,

$$\begin{aligned}\epsilon_i\phi_i(r) = &-\frac{\hbar^2}{2m}\nabla^2\phi_i(r) + \sum_{j>i}^{A}\int \phi_j^*(r')V(r,r')\phi_i(r)\phi_j(r')\,dr' \\ &-\sum_{j>i}^{A}\int \phi_j^*(r')V(r,r')\phi_i(r')\phi_j(r)\,dr'.\end{aligned} \tag{2.7}$$

The initial term in the equation is the kinetic energy contribution. The second term in Eq. 2.7 is the so-called "Hartree" potential term. The Hartree potential is an average field that the $i$th particle experiences due to all other particles in the system. This is a local potential depending solely on the one-body density, represented as

$\rho(\boldsymbol{r}) = \sum_{j=i}^{\Lambda} \phi_j^*(\boldsymbol{r})\phi_j(\boldsymbol{r})$. The third term is the exchange or "Fock" potential. The Fock potential is a non-local potential, $\rho(\boldsymbol{r}, \boldsymbol{r}') = \sum_{i=1}^{A} \phi_i^*(\boldsymbol{r}')\phi_i(\boldsymbol{r})$ reflecting the exchange interaction where particles can swap their positions while preserving the antisymmetrized nature of the overall wave function. Substituting these definitions, the Hartree-Fock equations become,

$$\epsilon_i\phi_i(r) = -\frac{\hbar^2}{2m}\nabla^2\phi_i(r) + U_H^{(i)}(r)\phi_i(r) - \int U_F^{(i)}(r, r')\phi_i(r')\, dr'. \tag{2.8}$$

The Hartree-Fock approach produces single-particle wave functions that make up the Slater determinant of the ground state. Due to the dependence of the potentials on the wave functions being solved, the equations become nonlinear and demand iterative, self-consistent solutions. This process requires introducing trial wave functions, formulating the potential, solving the Schrödinger equation to update the wave functions, and iterating until convergence is achieved.

## 2.2 The Skyrme Effective Interaction

Self-consistent mean-field models often employ effective interactions with free parameters. Given the short-range nature of nuclear interactions and the long wavelengths of single nucleon states, a Taylor expansion of zero-range interactions in momentum space is feasible. A local interaction with a spatial dependence $\delta(r - r')$ is used to approximate this expansion. Different symmetries, including translational, Galilean, rotational, and time-reversal invariance, are followed by the potential, which depends on nucleon positions, momenta, spins, and isospins. The local density approximation simplifies the Hartree-Fock equations significantly, leading to a mathematical representation of the exchange term that nearly resembles the direct term. One important method in developing mean-field models for nuclear property estimations has been building the Skyrme interaction. The Skyrme interaction is widely acknowledged as the major effective interaction used in these models [17]. The Skyrme Hamiltonian can be represented as follows:

$$\hat{H}_{\text{Skyrme}} = \hat{T} + \sum_{i<j} \hat{v}_{ij} + \sum_{i<j<k} \hat{v}_{ijk} + \hat{V}_{\text{Coul}}. \tag{2.9}$$

Here, $\hat{T}$ represents the kinetic energy operator,

$$\hat{T} = \sum_{i=1}^{N} \frac{\hat{p}_i^2}{2m}. \tag{2.10}$$

In the above equation, $\hat{p}_i = -\mathrm{i}\hbar\nabla_i$.$\hat{V}_{\text{Coul}}$ defines the Coulomb interaction between protons and $m$ in the denominator denotes the nucleon mass. Coulomb potential is defined as,

$$\hat{V}_{\text{Coul}} = \sum_{i<j} \frac{e^2}{|r_i - r_j|} \delta_{q_i p} \delta_{q_j p}. \tag{2.11}$$

The effective two-body interaction, which includes the effects of the three-body forces, is expressed as a density-dependent interaction,

$$\begin{aligned}
\hat{v}_{ij} = \hat{v}\left(r_i\sigma_i, r_j\sigma_j\right) =& t_0 \left(1 + x_0\hat{P}_\sigma\right) \delta\left(r_i - r_j\right) \\
&+ \frac{1}{6} t_3 \rho^\alpha \left(\frac{r_i + r_j}{2}\right) \left(1 + x_3\hat{P}_\sigma\right) \delta\left(r_i - r_j\right) \\
&+ \frac{1}{2} t_1 \left(1 + x_1\hat{P}_\sigma\right) \left\{\delta\left(r_i - r_j\right)\hat{k}^2 + \hat{k}'^2 \delta\left(r_i - r_j\right)\right\} \\
&+ t_2 \left(1 + x_2\hat{P}_\sigma\right) \hat{k}' \cdot \delta\left(r_i - r_j\right)\hat{k} \\
&+ \mathrm{i}W_0 \left(\hat{\sigma}_i + \hat{\sigma}_j\right) \cdot \left\{\hat{k}' \times \delta\left(r_i - r_j\right)\hat{k}\right\}.
\end{aligned} \tag{2.12}$$

Here, $\hat{\sigma}$ is the Pauli spin matrices, $\hat{P}_\sigma = \frac{1}{2}\left(1 + \hat{\sigma}_i \cdot \hat{\sigma}_j\right)$ defines the spin exchange operator. Relative wave vectors are defined as,

$$\hat{k} = \frac{\vec{\nabla}_i - \vec{\nabla}_j}{2\mathrm{i}}, \quad \hat{k}' = -\frac{\overleftarrow{\nabla}_i - \overleftarrow{\nabla}_j}{2\mathrm{i}}. \tag{2.13}$$

The operator $\hat{k}$ operates on spatial functions to the right, while the operator $\hat{k}'$ acts on spatial functions to the left. Additional parameters are adjusted to reproduce the fixed

structural characteristics of nuclear matter accurately. The EDF can be expressed as the expected value of the Skyrme Hamiltonian.

$$E_{\mathrm{SHF}}[\rho, \tau, j, s, T, \vec{\vec{J}}] = \left\langle \Phi \left| \hat{H}_{\mathrm{Skyrme}} \right| \Phi \right\rangle = \int dr \mathcal{H}(r). \tag{2.14}$$

In Eq. 2.14, $\rho$ represents the local density of nucleons, $\tau$ denotes the local kinetic energy density, and $s$ is the local spin density. The current density $j$ describes the flow of nucleons, while $T$ accounts for the contribution to the energy due to spin motion, known as the spin kinetic energy density. The spin-current tensor $\vec{\vec{J}}$ characterizes the spin-orbit interaction.

## 2.3 Time Dependent Hartree-Fock (TDHF) Equations

To study the behaviour of a nuclear system, the static Hartree-Fock equations can be expanded to the time domain by applying the time-dependent least action principle, similar to the static Hartree-Fock method. The temporal fluctuation of an action can be mathematically represented in the following manner,

$$\delta \int \Phi^*(r,t) \left( i\hbar \frac{\partial}{\partial t} - \hat{H} \right) \Phi(r,t) dt = 0. \tag{2.15}$$

By using a single Slater determinant as a trial function, we can derive the TDHF equation,

$$\mathrm{i}\hbar \frac{\partial \phi_i(r,t)}{\partial t} = \hat{H}\Phi(r,t). \tag{2.16}$$

In this work, we numerically solve the mean-field dynamics using the TDHF code [18, 13] for Eq.2.16 with the SLy4d Skyrme EDF [19]. This TDHF code uses basis-spline discretization for high numerical accuracy, makes no assumptions on geometrical symmetry such as axial or reflection symmetries, and incorporates the full EDF. The Coulomb trajectory determines the initial approach up to $R_0$, where the strong nuclear interaction between nuclei becomes effective. Beyond $R_0$, the system dynamics are governed by the TDHF equations, which are solved self-consistently, starting with

an initial guess of orthonormal single-particle states until the convergence criteria are met.

In this work, we studied the following nuclear systems: $^{58}$Fe + $^{208}$Pb reaction with $E_{\text{c.m.}}$ = 238.5 MeV, $^{36}$S + $^{238}$U reaction with $E_{\text{c.m.}}$ = 151.1 MeV, $^{64}$Ni + $^{130}$Te reaction with $E_{\text{c.m.}}$ = 184.3 MeV and $^{206}$Pb + $^{118}$Sn reaction with $E_{\text{c.m.}}$ = 436.8 MeV. These systems were selected due to their relevance in understanding various aspects of nuclear reactions, such as multi-nucleon transfer processes, quasi-fission dynamics, and the production of exotic nuclei. The $^{58}$Fe + $^{208}$Pb system helps evaluate the interaction processes between mid-mass nuclei and heavy targets, highlighting transfer and quasi-fission processes. The $^{36}$S + $^{238}$U system is particularly interesting for studying the dynamics involving very heavy nuclei and shell effects in quasi-fission [20]. The $^{64}$Ni + $^{130}$Te system allows us to explore the behaviour of neutron-rich and proton-rich interactions, which are crucial for producing exotic nuclei far from stability [21]. Finally, the $^{206}$Pb + $^{118}$Sn system is important for studying neutron-proton asymmetry and its influence on reaction dynamics and nucleon transfer mechanisms [22]. The outcomes of the TDHF computations for these systems will be given and discussed in the subsequent section.

### 2.4 Results of TDHF Calculations for Selected Heavy-Ion Systems

For the TDHF solutions of reaction systems, static calculations are performed for each collision partner in the reaction system. These static calculations model the ground state properties of each nucleus. The static solutions for the collision partners are then placed in a numerical box sized 60 x 60 x 36 fm in the (x-y-z) coordinates for dynamic calculations. Each nucleus is given a boost towards the other according to their Coulomb trajectories. The dynamic calculations continue until the colliding nuclei reach a separation distance after their interactions, and at this point, the strong interaction between the nuclei ceases.

In Fig. 2.1, each system's mass densities are presented at different time windows: the beginning of the dynamical calculations, initial neck formation, and final neck formation before and after separation. From the mass densities, the placement of the

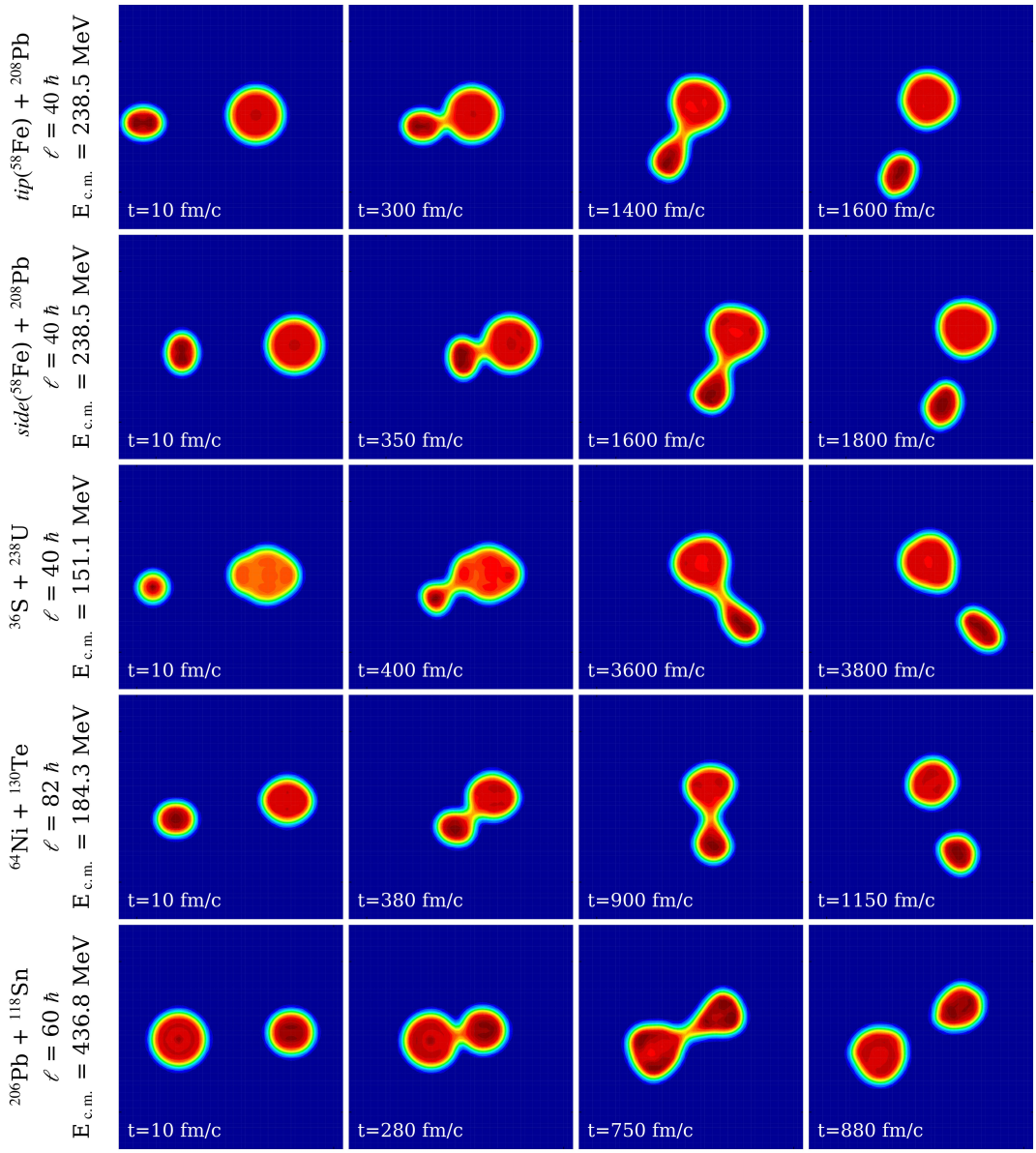


Figure 2.1: Snapshots of density profiles for each system at different times on the reaction plane.

nuclei inside the numerical box and their deformation throughout the process can be observed.

From the initial interaction to the point after the separation of two nuclei, the result of the TDHF calculations for each system's observables is presented in TDHF tables and drift plots. On TDHF tables, $\ell_i$ denotes the initial angular momentum of the system, which can be defined in terms of impact parameter $b$ as given by Eq. 1.1. $Z_1^f$, $A_1^f$

represents the final proton and mass numbers of projectile-like fragment and $Z_2^f$, $A_2^f$ represents the target-like fragment. $\ell_f$ indicates the final angular momentum of the system, while $TKE$ is the final total kinetic energy of fragments. The final centre-of-mass angle of the reaction system is denoted with $\theta_{c.m.}$, where we can calculate scattering angles of reaction partners in the laboratory frame as,

$$\tan\theta_1^{\text{lab}} = \frac{\sin\theta_{\text{c.m.}}}{\sqrt{\frac{A_1^f A_1^f}{A_2^f A_2^f}\frac{E_{\text{cm}}}{\text{TKE}}} + \cos\theta_{\text{c.m.}}}, \tag{2.17}$$

and

$$\tan\theta_2^{\text{lab}} = \frac{\sin\theta_{\text{c.m.}}}{\sqrt{\frac{A_1^i A_2^f}{A_1^f A_2^i}\frac{E_{\text{c.m.}}}{\text{TKE}}} - \cos\theta_{\text{c.m.}}}. \tag{2.18}$$

The drift path plots illustrate the movement of the reaction system on the N-Z plane, with the direction of the reaction's evolution over time indicated by an arrow. Points labelled A, B, and C will be utilized in the subsequent chapters to compute average values of reduced curvature parameters $\alpha$ and $\beta$. The N-Z-t graphs additionally indicate the respective times of these points in the reaction dynamics. In this work, the entrance channel charge asymmetries ($\delta = \frac{N-Z}{A}$) vary across the collision partners of all the reaction systems. This leads to a quick transition to charge equilibrium at the initial phase of the reaction. Once the charge equilibrium point has been reached, the rate of nucleon transfer decreases, and the reaction system progresses along the iso-scalar line with a nearly uniform charge asymmetry. The iso-scalar line is a straight path that connects the reaction partner with lower mass to the reaction partner with higher mass. This line passes via the mass symmetry point, which is defined as,

$$N_0 = (N_1 + N_2)/2, \qquad Z_0 = (Z_1 + Z_2)/2. \tag{2.19}$$

In $^{58}$Fe + $^{208}$Pb reaction system, the ground state of the $^{58}$Fe nuclei has prolate deformation as shown on Fig. 2.1, which requires to study two different collision geometries. We define collision geometries as a $tip$ when the principal deformation axis of

the deformed partner lies on the beam direction and $side$, as the principal deformation axis is orthogonal to the beam direction. Figure 2.2 and Fig. 2.3 show results for $Fe$-like fragments in the $^{58}$Fe + $^{208}$Pb reaction system with $E_{\text{c.m.}}$ = 238.5 MeV in tip and side collision geometries with an initial angular momentum of $\ell = 40\hbar$, which shows reasonable drift behaviour for further calculations. Fig. 2.2(a) and Fig. 2.3(a) show the drift path of the reaction system indicated with magenta lines. Both systems show similarities in drift paths. Initial charge asymmetries of collision partners are, $^{58}$Fe is $\delta = 0.10$ and $^{208}$Pb is $\delta = 0.21$. To reach charge equilibrium, $Fe$-like fragments lose protons and drift towards the iso-scalar line, represented by solid black lines with dashed ends, which makes an angle about $\phi = 33.1^{\circ}$ from the neutron axis on the N-Z plane. On the iso-scalar line, drift continues through the symmetry point $(N_0, Z_0)$ with a nearly constant charge asymmetry of $0.17$. In Fig. 2.2(b) and Fig. 2.3(b), neutron and proton number change in time on the drift path is presented.

Results of the TDHF calculations for these systems are shown in Table 2.1, which shows similarities for tip and side collision geometries. The initial angular momentum range is $40\hbar \leq \ell \leq 240\hbar$. Below $\ell = 40\hbar$, collision partners do not separate in the calculations, assuming the system is fused. Above $\ell = 240\hbar$, collision becomes an elastic one. $\ell = 20\hbar$ intervals optimize the calculation time whilst preserving the gradient in reaction dynamics.

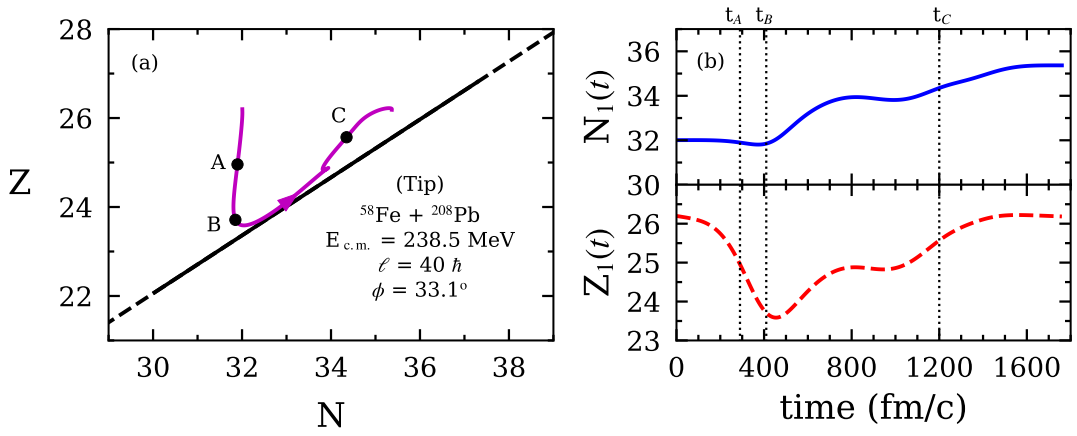


Figure 2.2: (a) Drift path for the $Fe$-like fragments and (b) the mean neutron and proton numbers of $Fe$-like fragments in the $^{58}$Fe+$^{208}$Pb reaction with $E_{\text{c.m.}}$ = 238.5 MeV in the tip orientation of the $^{58}$Fe for $\ell = 40\hbar$.

Table 2.1: TDHF results for $^{58}$Fe + $^{208}$Pb reaction with $E_{\text{c.m.}}$ = 238.5 MeV.

| - | $\ell_i$ ($\hbar$) | $b(fm)$ | $Z_1^f$ | $A_1^f$ | $Z_2^f$ | $A_2^f$ | $\ell_f$ ($\hbar$) | $TKE(MeV)$ | $\theta_{c.m.}(deg.)$ | $\theta_1^{lab}(deg.)$ | $\theta_2^{lab}(deg.)$ |
|---|---|---|---|---|---|---|---|---|---|---|---|
| | 40 | 1.8 | 26.2 | 61.5 | 81.8 | 204.5 | 35.1 | 191.5 | 105.5 | 86.7 | 35.7 |
| | 60 | 2.6 | 26.6 | 62.4 | 81.4 | 203.6 | 49.4 | 189.5 | 93.1 | 74.7 | 41.6 |
| | 80 | 3.5 | 25.5 | 59.6 | 82.5 | 206.4 | 65.7 | 187.0 | 103.2 | 84.6 | 36.0 |
| | 100 | 4.4 | 25.8 | 58.5 | 82.2 | 207.5 | 99.5 | 231.7 | 107.8 | -88.7 | 35.9 |
| | 120 | 5.3 | 26.0 | 58.2 | 82.0 | 207.8 | 123.2 | 236.9 | 99.6 | 83.4 | 40.2 |
| tip($^{58}$Fe) | 140 | 6.2 | 26.0 | 58.1 | 82.0 | 207.9 | 143.7 | 237.5 | 91.3 | 75.6 | 44.3 |
| | 160 | 7.0 | 26.0 | 58.0 | 82.0 | 208.0 | 163.0 | 237.8 | 84.1 | 69.0 | 47.9 |
| | 180 | 7.9 | 26.0 | 58.0 | 82.0 | 208.0 | 182.3 | 238.0 | 77.7 | 63.2 | 51.1 |
| | 200 | 8.8 | 26.0 | 58.0 | 82.0 | 208.0 | 202.2 | 238.0 | 71.9 | 58.2 | 54.0 |
| | 220 | 9.7 | 26.0 | 58.0 | 82.0 | 208.0 | 222.6 | 238.1 | 66.8 | 53.8 | 56.5 |
| | 240 | 10.5 | 26.0 | 58.0 | 82.0 | 208.0 | 242.3 | 238.2 | 62.4 | 50.1 | 58.8 |
| | 40 | 1.8 | 27.4 | 64.9 | 80.6 | 201.1 | 33.3 | 190.3 | 100.5 | 81.1 | 38.8 |
| | 60 | 2.6 | 25.5 | 59.4 | 82.5 | 206.6 | 47.0 | 184.3 | 117.7 | -80.8 | 29.2 |
| | 80 | 3.5 | 25.5 | 58.7 | 82.5 | 207.3 | 74.1 | 217.5 | 116.3 | -80.6 | 31.2 |
| | 100 | 4.4 | 25.9 | 58.4 | 82.1 | 207.6 | 95.8 | 235.3 | 110.2 | -86.2 | 34.9 |
| | 120 | 5.3 | 26.0 | 58.2 | 82.0 | 207.8 | 116.4 | 236.6 | 101.0 | 84.8 | 39.4 |
| side($^{58}$Fe) | 140 | 6.2 | 26.0 | 58.1 | 82.0 | 207.9 | 136.4 | 237.0 | 92.7 | 76.8 | 43.6 |
| | 160 | 7.0 | 26.0 | 58.0 | 82.0 | 208.0 | 156.9 | 237.2 | 85.2 | 70.0 | 47.3 |
| | 180 | 7.9 | 26.0 | 58.0 | 82.0 | 208.0 | 176.8 | 237.5 | 78.7 | 64.1 | 50.6 |
| | 200 | 8.8 | 26.0 | 58.0 | 82.0 | 208.0 | 197.4 | 237.6 | 72.8 | 59.0 | 53.5 |
| | 220 | 9.7 | 26.0 | 58.0 | 82.0 | 208.0 | 218.2 | 237.8 | 67.6 | 54.5 | 56.1 |
| | 240 | 10.5 | 26.0 | 58.0 | 82.0 | 208.0 | 238.6 | 237.9 | 63.1 | 50.6 | 58.4 |

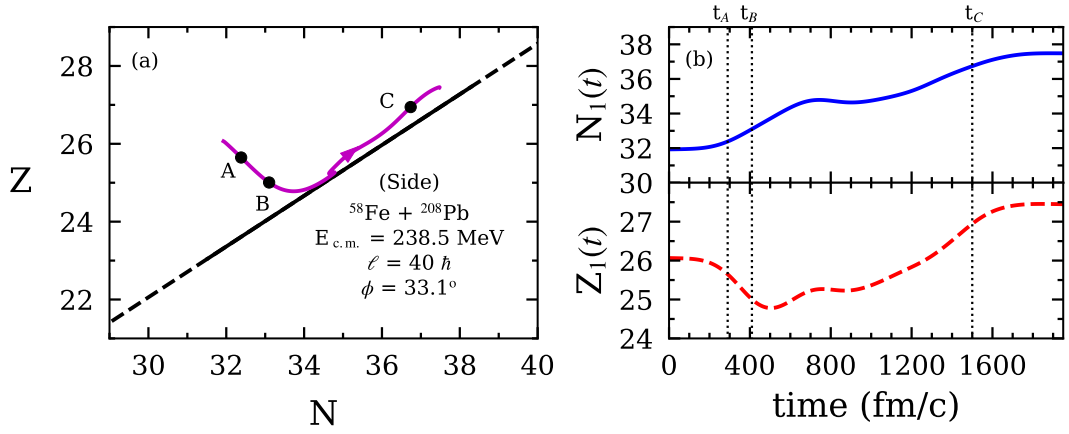


Figure 2.3: (a) Drift path for the $Fe$-like fragments and (b) the mean neutron and proton numbers of $Fe$-like fragments in the $^{58}$Fe+$^{208}$Pb reaction with $E_{\text{c.m.}}$ = 238.5 MeV in the side orientation of the $^{58}$Fe for $\ell = 40\hbar$.

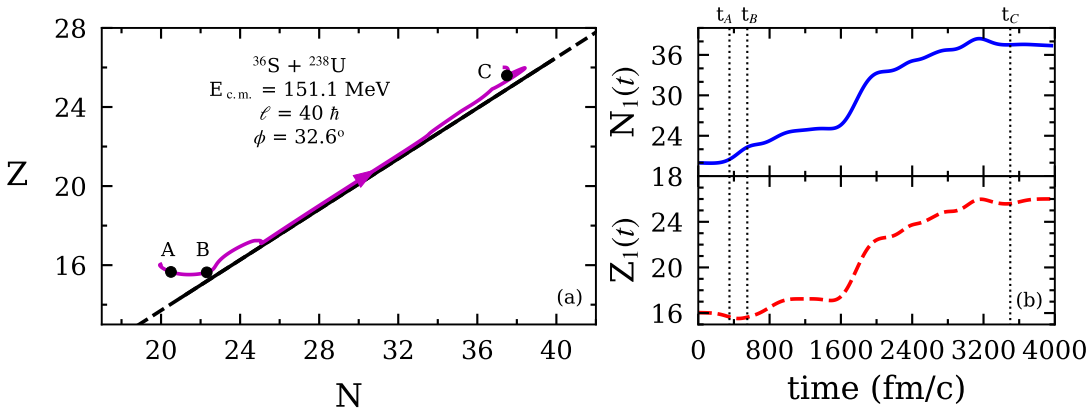


Figure 2.4: (a) Drift path for the $S$-like fragments and (b) the mean neutron and proton numbers of $S$-like fragments in the $^{36}$S + $^{238}$U reaction with $E_{\text{c.m.}}$ = 151.1 MeV for $\ell = 40\hbar$.

The reaction system featuring $^{36}$S + $^{238}$U consists of a projectile $^{36}$S with no ground state deformation and a target partner $^{238}$U with a prolate deformation in its ground state [23]. This can be observed in Figure 2.1. The collision geometry directly affects the reaction dynamics when reaction partners exhibit ground state deformation. In this particular instance, our initial computations on various collision geometry configurations indicated that, at $E_{\text{c.m.}}$ = 151.1 MeV, there was minimal nucleon transfer, except for the tip orientation of the $^{238}$U nuclei. Therefore, we exclusively utilized tip collision geometry for subsequent calculations on this system. Figure. 2.4(a) displays the trajectory of the system's motion when the initial angular momentum is $\ell = 40\hbar$. This trajectory is suitable for subsequent calculations.

The initial charge asymmetries of the collision partners are as follows: $^{36}$S has a charge asymmetry of $\delta = 0.11$, while $^{238}$U has a charge asymmetry of $\delta = 0.23$. On Fig. 2.4(b) $S$-like fragments acquire neutrons while losing protons to reach charge equilibrium on the iso-scalar line with a charge asymmetry of $\delta = 0.20$. The iso-scalar line makes an angle of $\phi = 32.6°$ from the neutron axis on the N-Z plane. Drift continues along the iso-scalar line. Initial angular momentum ranges $\ell = 34\hbar$ to $\ell = 50\hbar$ is considered for this system where fusion is observed up to $\ell = 34\hbar$. After $\ell = 40\hbar$, quasielastic components becomes dominant and beyond $\ell = 50\hbar$, collision becomes elastic as can be observed on Table 2.2.

Table 2.2: TDHF results for the $^{36}$S + $^{238}$U reaction with $E_{\text{c.m.}}$ = 151.1 MeV.

| $\ell_i$ ($\hbar$) | $b(fm)$ | $Z_1^f$ | $A_1^f$ | $Z_2^f$ | $A_2^f$ | $\ell_f$ ($\hbar$) | $TKE(MeV)$ | $\theta_{c.m.}(deg.)$ | $\theta_1^{lab}(deg.)$ | $\theta_2^{lab}(deg.)$ |
|---|---|---|---|---|---|---|---|---|---|---|
| 34 | 2.3 | 26.7 | 66.0 | 81.3 | 208.0 | 27.2 | 179.4 | 87.7 | 76.4 | 59.3 |
| 35 | 2.3 | 26.9 | 66.2 | 81.1 | 207.8 | 30.2 | 177.5 | 93.5 | 81.9 | 55.1 |
| 36 | 2.4 | 27.3 | 67.4 | 80.7 | 206.6 | 28.8 | 178.3 | 96.4 | 84.6 | 53.4 |
| 37 | 2.5 | 27.1 | 66.2 | 80.9 | 207.8 | 29.1 | 174.9 | 82.7 | 71.5 | 62.6 |
| 38 | 2.5 | 27.3 | 66.4 | 80.7 | 207.6 | 29.6 | 172.2 | 64.1 | 54.4 | 77.1 |
| 39 | 2.6 | 26.0 | 63.0 | 82.0 | 211.0 | 31.2 | 167.6 | 36.4 | 30.5 | -77.7 |
| 40 | 2.7 | 26.0 | 63.3 | 82.0 | 210.7 | 32.2 | 169.1 | 46.5 | 39.2 | -88.6 |
| 41 | 2.7 | 16.3 | 39.5 | 91.7 | 234.5 | 4.5 | 124.7 | 141.1 | -46.2 | 19.0 |
| 42 | 2.8 | 15.6 | 38.0 | 92.4 | 236.0 | 14.8 | 126.5 | 136.7 | -50.9 | 21.0 |
| 44 | 2.9 | 15.0 | 36.6 | 93.0 | 237.4 | 25.1 | 125.1 | 132.9 | -55.0 | 22.5 |
| 46 | 3.1 | 15.1 | 36.0 | 92.9 | 238.0 | 35.0 | 128.7 | 129.7 | -58.3 | 24.1 |
| 48 | 3.2 | 15.4 | 35.9 | 92.6 | 238.1 | 46.2 | 138.0 | 127.2 | -60.7 | 25.7 |
| 50 | 3.3 | 15.7 | 36.0 | 92.3 | 238.0 | 53.8 | 144.8 | 125.3 | -62.6 | 27.0 |

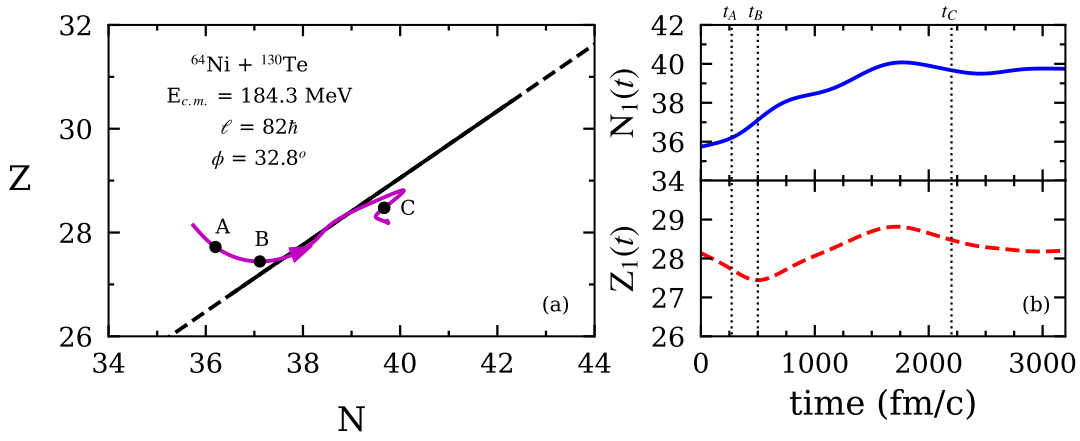


Figure 2.5: (a) Drift path for the $Ni$-like fragments and (b) the mean neutron and proton numbers of $Ni$-like fragments in the $^{64}$Ni+$^{130}$Te reaction with $E_{\text{c.m.}}$ = 184.3 MeV for $\ell = 82\hbar$.

For the $^{64}$Ni + $^{130}$Te reaction system, no ground state deformation is observed on collision partners, for which both nuclei are nearly spherical. The initial angular momentum range of $82\hbar \leq \ell \leq 180\hbar$ is considered. The system is fused below $\ell < 82\hbar$, and beyond $\ell > 180\hbar$, fragments elastically scatter. Figure 2.5(a) illustrates the drift path of the reaction system, shown by magenta lines. The initial charge asymmetry of $^{64}$Ni is $\delta = 0.13$, while $^{130}$Te has a charge asymmetry of $\delta = 0.20$. On

Fig. 2.5(b) after the initial contact, $Ni$-like fragments show a distinct trend of gaining neutrons and losing protons to reach charge equilibrium with a charge asymmetry of $0.16$ on the iso-scalar line, which is making an angle of approximately $\phi = 32.8^{\circ}$ relative to the neutron axis on the N-Z plane.

Table 2.3: TDHF results for the $^{64}$Ni + $^{130}$Te reaction with $E_{\text{c.m.}}$ = 184.3 MeV.

| $\ell_i$ ($\hbar$) | $b(fm)$ | $Z_1^f$ | $A_1^f$ | $Z_2^f$ | $A_2^f$ | $\ell_f$ ($\hbar$) | $TKE(MeV)$ | $\theta_{c.m.}(deg.)$ | $\theta_1^{lab}(deg.)$ | $\theta_2^{lab}(deg.)$ |
|---|---|---|---|---|---|---|---|---|---|---|
| 82 | 4.2 | 28.2 | 68.0 | 51.8 | 126.0 | 69.4 | 135.5 | 49.4 | 31.2 | 58.6 |
| 84 | 4.3 | 27.7 | 65.5 | 52.3 | 128.5 | 66.9 | 145.7 | 75.3 | 49.8 | 48.6 |
| 86 | 4.4 | 27.6 | 65.3 | 52.4 | 128.7 | 68.5 | 145.1 | 79.6 | 52.9 | 46.6 |
| 88 | 4.5 | 27.1 | 63.9 | 52.9 | 130.1 | 73.7 | 154.9 | 92.7 | 63.9 | 41.2 |
| 90 | 4.6 | 27.2 | 63.8 | 52.8 | 130.2 | 80.0 | 160.4 | 92.7 | 64.3 | 41.7 |
| 92 | 4.7 | 27.6 | 64.0 | 52.4 | 130.0 | 88.0 | 172.5 | 92.7 | 65.2 | 42.7 |
| 94 | 4.8 | 27.8 | 64.0 | 52.2 | 130.0 | 93.0 | 177.4 | 92.7 | 65.5 | 43.1 |
| 96 | 4.9 | 27.9 | 64.1 | 52.1 | 129.9 | 96.8 | 179.8 | 93.5 | 66.3 | 43.0 |
| 98 | 5.0 | 27.9 | 64.1 | 52.1 | 129.9 | 99.3 | 181.0 | 93.0 | 66.0 | 43.3 |
| 100 | 5.1 | 27.9 | 64.1 | 52.1 | 129.9 | 101.3 | 181.5 | 92.3 | 65.4 | 43.7 |
| 110 | 5.7 | 28.0 | 64.0 | 52.0 | 130.0 | 113.5 | 183.1 | 88.0 | 62.1 | 45.9 |
| 120 | 6.2 | 28.0 | 64.0 | 52.0 | 130.0 | 123.5 | 183.5 | 83.6 | 58.7 | 48.1 |
| 140 | 7.2 | 28.0 | 64.0 | 52.0 | 130.0 | 143.4 | 183.8 | 75.4 | 52.4 | 52.3 |
| 160 | 8.2 | 28.0 | 64.0 | 52.0 | 130.0 | 162.8 | 184.0 | 68.5 | 47.3 | 55.7 |
| 180 | 9.3 | 28.0 | 64.0 | 52.0 | 130.0 | 182.6 | 184.1 | 62.5 | 42.9 | 58.7 |

For the $^{206}$Pb+$^{118}$Sn reaction system, no ground state deformation is observed. Initial charge asymmetries of collision partners are, $^{206}$Pb is $\delta = 0.20$ and $^{118}$Sn is $\delta = 0.15$. After the initial contact, the system moves towards the charge equilibrium with a charge asymmetry of $\delta = 0.19$ on the iso-scalar line, which makes an angle about $\phi = 33.0^{\circ}$ from the neutron axis on the N-Z plane presented in Fig. 2.6(a). In Figure2.6(b), until charge equilibrium is reached, the projectile $^{206}$Pb fragment loses neutrons while gaining protons from the target. This behaviour differs from other systems studied in this work, where the target is heavier, leading to initial charge equilibration by the projectile gaining neutrons and losing protons to the target partner. The initial angular momentum range $60\hbar \leq \ell \leq 260\hbar$ is utilized where below $\ell = 60\hbar$ collision partners are fused. Above $\ell = 260\hbar$ collision system becomes elastic.

Detailed microscopic insights into the time development of single-particle wave functions are provided by the TDHF theory, which has shown to be a powerful tool for

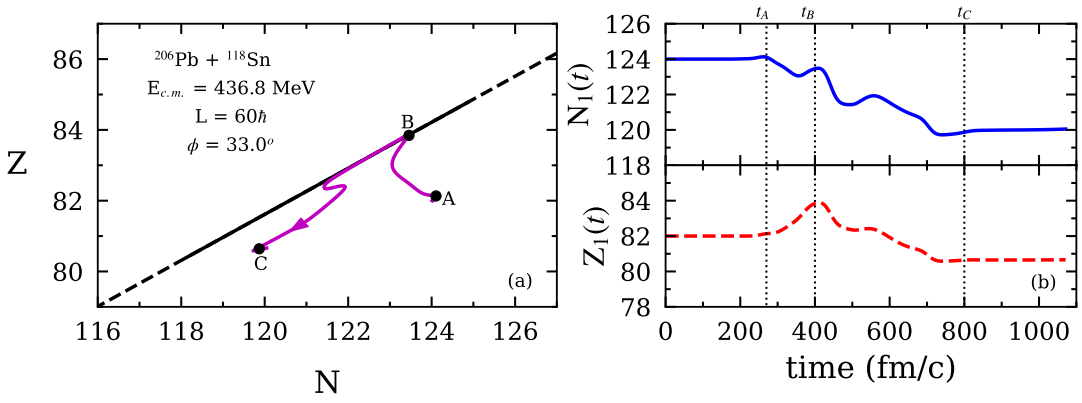


Figure 2.6: (a) Drift path for the $Pb$-like fragments and (b) the mean neutron and proton numbers of $Pb$-like fragments in the $^{206}$Pb+$^{118}$Sn reaction with $E_{\text{c.m.}}$ = 436.8 MeV for $\ell = 60\hbar$.

Table 2.4: TDHF results for the $^{206}$Pb + $^{118}$Sn reaction with $E_{\text{c.m.}}$ = 436.8 MeV.

| $\ell_i$ ($\hbar$) | $b(fm)$ | $Z_1^f$ | $A_1^f$ | $Z_2^f$ | $A_2^f$ | $\ell_f$ ($\hbar$) | $TKE(MeV)$ | $\theta_{c.m.}(deg.)$ | $\theta_1^{lab}(deg.)$ | $\theta_2^{lab}(deg.)$ |
|---|---|---|---|---|---|---|---|---|---|---|
| 60 | 1.5 | 80.7 | 200.7 | 51.3 | 123.3 | 52.7 | 329.8 | 144.9 | 27.1 | 16.0 |
| 80 | 2.0 | 80.9 | 201.3 | 51.1 | 122.7 | 68.9 | 332.5 | 136.0 | 29.6 | 20.1 |
| 100 | 2.5 | 81.6 | 202.8 | 50.4 | 121.2 | 83.3 | 330.7 | 127.7 | 30.3 | 23.9 |
| 120 | 3.0 | 82.0 | 203.5 | 50.0 | 120.5 | 98.2 | 337.1 | 120.4 | 30.8 | 27.4 |
| 140 | 3.5 | 82.3 | 204.4 | 49.7 | 119.6 | 114.5 | 352.2 | 115.3 | 31.1 | 30.2 |
| 160 | 4.0 | 82.6 | 205.5 | 49.4 | 118.5 | 139.0 | 377.8 | 110.6 | 31.6 | 33.2 |
| 180 | 4.5 | 82.3 | 205.5 | 49.7 | 118.5 | 168.9 | 406.4 | 106.8 | 32.3 | 35.8 |
| 200 | 5.1 | 82.1 | 206.0 | 49.9 | 118.0 | 196.9 | 428.7 | 104.0 | 32.5 | 37.8 |
| 220 | 5.6 | 82.0 | 206.0 | 50.0 | 118.0 | 219.9 | 433.9 | 99.7 | 31.9 | 40.1 |
| 240 | 6.1 | 82.0 | 206.0 | 50.0 | 118.0 | 241.7 | 434.9 | 95.2 | 31.0 | 42.4 |
| 260 | 6.6 | 82.0 | 206.0 | 50.0 | 118.0 | 262.2 | 435.4 | 90.8 | 30.0 | 44.5 |

explaining nuclear dynamics. This has been important to understanding various nuclear phenomena, ranging from collective excitations to heavy-ion collisions. The strength of this framework is its nature to predict things without including more empirical parameters once the EDF is defined. This results in a unified description of such static properties as binding energies and deformations with dynamic processes such as fusion and QF.

However, TDHF is subject to substantial limitations due to the mean-field approximation. The mean-field approximation assumes particles move in the average field

created by all other particles, neglecting extensive two-body correlations. Generally, TDHF underestimates fluctuations and correlations in one-body observables, and the method is optimized to predict average quantities because of its deterministic nature.

Beyond mean-field approaches, like the SMF theory [24], have been developed to address these limitations. The SMF extends TDHF by including stochastic ingredients to follow the influence of initial state fluctuations and their time evolution and introduces one-body dissipation and fluctuation mechanisms in a way that respects the quantum fluctuation-dissipation relations.

The following chapter will briefly review beyond-mean-field approaches and describe the SMF theory. We calculate the transport coefficients of the reaction systems using the TDHF solutions presented in the current chapter. With the fluctuations included, we can give a more realistic picture of the outcome of the reactions.

# CHAPTER 3

# SMF THEORY AND ITS APPLICATION TO THE MNT REACTIONS

Studying the mechanics of MNT reactions requires an extensive theoretical framework to model these complex events effectively. Reaction dynamics are explained using the TDHF theory, which has been widely used to analyze MNT reactions [7, 8, 25, 26]. The TDHF framework allows for calculation of dynamical observables such as the average charge and mass of a fragment, as well as the average kinetic energy loss resulting from one-body dissipation [27]. While TDHF theory has many benefits, it is unable to account for fluctuations and deviations in fragment mass and charge distributions. To get around this restriction, one must go beyond the mean-field approximation [24, 28].

## 3.1 Beyond Mean-Field Approaches

The extended variational theory presented by Balian and Vénéroni [29] is the basis for the time-dependent random phase approximation (TDRPA), significantly enhancing the description of MNT reactions. The TDRPA formula considers the fluctuations and correlations of one-body observables around the TDHF average trajectory by including dispersions into a single Slater determinant. The approach has been successfully applied to deep-inelastic collisions involving $^{16}\mathrm{O}+{}^{16}\mathrm{O}$ [30] and $^{40}\mathrm{Ca}+{}^{40}\mathrm{Ca}$ [31], resulting in significant enhancements in the description. However, the current TDRPA formula is not suited for asymmetric systems, which limits its use for extensive investigations, including various combinations of projectiles and targets [32].

S. Ayik introduced a novel method for describing MNT reactions that goes beyond mean-field fluctuations and correlations: the SMF approach [24]. This method uti-

lizes time-dependent mean-field solutions to describe the quantum many-body problem. The incorporation of initial mean-field fluctuations in this context is similar to the derivation of quantum mechanics from Brownian particles, as described by Nelson in 1966 [33]. Beyond one-body fluctuations and correlations, the SMF approach featured a simplified Bogoliubov-Born-Green-Kirkwood-Yvon (BBGKY) hierarchy [34]. When the fluctuations are small, the SMF approach is analytically equivalent to the TDRPA formula [24, 28], and is especially well-suited for asymmetric systems.

Recent developments have led to improvements in the SMF description. The initial methodology employed a semiclassical approach, utilizing the Wigner transformation and the Markov approximation, as shown in the references [35, 36, 37, 38, 39]. Using the completeness relation [40], which depends on single-particle orbitals obtained from mean-field theory, a quantum-based formula for the diffusion coefficient was proposed and refined in reference [41]. Quantal expressions were applied to head-on collisions of $^{238}$U $+^{238}$ U [42] and to central collisions of symmetric systems, namely $^{28}$O$+^{28}$O, $^{40,48}$Ca$+^{40,48}$Ca, and $^{56}$Ni$+^{56}$Ni, occurring just below the Coulomb barrier. Subsequently, the quantal diffusion model was expanded to incorporate non-central collisions [43].

## 3.2 Description of the SMF Theory

### 3.2.1 Derivation of the Langevin Equation for Macroscopic Variables

Starting with a given initial state, the standard TDHF equation determines the time evolution of the single-particle density matrix. While the standard approach estimates the overall development of collective movement, it does not include the impact of variations around the average value of collective motion. In contrast to the standard mean-field theory, the SMF theory incorporates a stochastic method that considers the system's initial state's quantum and thermal density fluctuations. Quantum and thermal fluctuations are determined by the initial conditions. To account for these fluctuations, quantal calculations are carried out by averaging over ensembles with the suitable distribution of various initial conditions.

The initial density fluctuations are simulated as density matrices rather than a single density matrix. Thus, a superposition of Slater determinants is considered instead of considering a single Slater determinant. In the SMF approach, an element of the ensemble of single-particle density matrices, represented by the index $\lambda$, includes quantum and thermal fluctuations in the initial state defined as,

$$\rho_a^\lambda(\vec{r},\vec{r}\,',t) = \sum_{ij} \phi_i(\vec{r},t;\lambda)\langle i|\rho_a^\lambda(t_0)|j\rangle\phi_j^*(\vec{r}\,',t;\lambda). \tag{3.1}$$

Here, $i,j$ subscripts represent the index of singe-particle wave functions $\phi_i(\vec{r},t;\lambda)$, $a$ subscript goes between the type of nucleon and $\rho_{ij}^\lambda = \left\langle i \left| \rho_a^\lambda(t_0) \right| j \right\rangle$ is the time-independent element of the density matrix defined by the initial conditions. The fundamental assumption in the SMF approach is that the density matrix elements are independent random numbers. The mean values of these random numbers, which follow Gaussian distributions, are given by,

$$\overline{\rho_{ij}^\lambda} = \overline{\langle i \left| \rho_a^\lambda(t_0) \right| j\rangle} = \delta_{ij} n_j, \tag{3.2}$$

while the variances of the elements corresponding to fluctuations in the density are given by,

$$\overline{\langle i \left| \delta\rho_a^\lambda(t_0) \right| j\rangle \left\langle j' \left| \delta\rho_b^\lambda(t_0) \right| i' \right\rangle} = \frac{1}{2}\delta_{ab}\delta_{ii'}\delta_{jj'}\left[n_i\left(1-n_j\right) + n_j\left(1-n_i\right)\right]. \tag{3.3}$$

In this context, $n_j$ denotes the occupation factors of the initial wave functions. At absolute zero temperature, the values can only be 1 or 0. However, the Fermi-Dirac distribution determines the values at temperatures above absolute zero. The ensemble's mean-field Hamiltonian is used by the TDHF equation to calculate the single-particle wave function in each event.

$$i\hbar\frac{\partial}{\partial t}\phi_j(\vec{r},t;\lambda) = h\left[\rho_a^\lambda(t)\right]\phi_j(\vec{r},t;\lambda). \tag{3.4}$$

When projectile-like and target-like nuclei form a two-center structure in collision

reactions like QF and DIC, the window between the colliding partners can be chosen appropriately to define collective variables like the mass and charge asymmetry, relative distance, and relative momentum of the projectile-like and target-like nuclei [37, 38]. The geometry of the di-nuclear system is represented in Fig. 3.1 in the CM reference system, where the collision axis is the x-axis, and the equation for the window plane is written as,

$$(y - y_0)\sin\theta + (x - x_0)\cos\theta = 0, \tag{3.5}$$

and for the symmetry axis,

$$(y - y_0)\cos\theta - (x - x_0)\sin\theta = 0. \tag{3.6}$$

In the above equations, $(x_0, y_0)$ marks the center of the window plane, and $\theta$ measures the angle between the symmetry and collision axes.

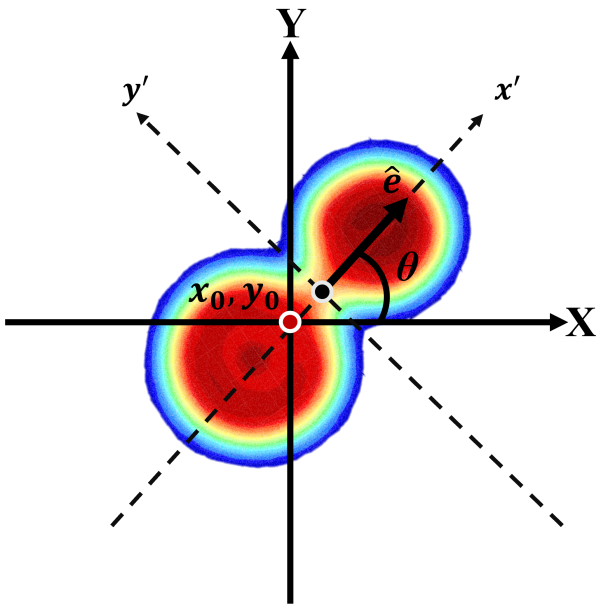


Figure 3.1: Representation of the coordinate system for a di-nuclear system with a finite impact parameter. The symmetry axis is labelled as $x'$, and the window plane between the collision partners is labelled as $y'$. The normal vector of the window plane is represented with $\hat{e}$.

In this case, the macroscopic variables are the nucleus's neutron and proton numbers on one side of the window. The neutron and proton densities are expressed in terms of these macroscopic variables, $\rho_n^\lambda(\vec{r},t)$ and $\rho_p^\lambda(\vec{r},t)$ for the event $\lambda$ generated by the SMF theory, are defined as:

$$\begin{pmatrix} N_1^\lambda(t) \\ Z_1^\lambda(t) \end{pmatrix} = \int d^3r\Theta\left\{[x-x_0(t)]\cos\theta + [y-y_0(t)]\sin\theta\right\} \begin{pmatrix} \rho_n^\lambda(\vec{r},t) \\ \rho_p^\lambda(\vec{r},t) \end{pmatrix}. \tag{3.7}$$

In the Eq. 3.7, $\Theta(f(x))$ denotes the Heaviside step function. The SMF theory claims that the stochastic Langevin dynamics drive the temporal evolution of collective variables. The temporal variations in the number of protons and neutrons within the projectile-like nuclei are described by the following expression:

$$\frac{d}{dt}\begin{pmatrix} N_1^\lambda(t) \\ Z_1^\lambda(t) \end{pmatrix} = \int d^3r\delta\left(x'\right)\dot{\mathrm{x}}'\begin{pmatrix} \rho_n^\lambda(\vec{\mathrm{r}},t) \\ \rho_p^\lambda(\vec{\mathrm{r}},t) \end{pmatrix} + \int d^3r\Theta\left(x'\right)\frac{\partial}{\partial t}\begin{pmatrix} \rho_n^\lambda(\vec{\mathrm{r}},t) \\ \rho_p^\lambda(\vec{\mathrm{r}},t) \end{pmatrix}, \tag{3.8}$$

where, $x'$ is the point on the window plane and $\dot{x'}$ is the velocity and $\delta(x')$ is the delta function. The continuity equation for the current $j$ and the density $\rho$ is written as,

$$\frac{\partial}{\partial t}\rho_\alpha^\lambda(\vec{r},t) = -\vec{\nabla}\cdot\vec{j}_\alpha^\lambda(\vec{r},t) = -\left[\partial_x j_{x,\alpha}^\lambda(\vec{r},t) + \partial_y j_{\mathrm{y},\alpha}^\lambda(\vec{r},t) + \partial_z j_{\mathrm{z},\alpha}^\lambda(\vec{r},t)\right]. \tag{3.9}$$

In the given equation, $\alpha$ denotes the type of nucleon, whereas $\lambda$ indicates the label assigned to the event. Equation 3.9 can be utilized to obtain the stochastic Langevin equation that describes the change in neutron and proton numbers.

$$\begin{aligned} \frac{d}{dt}\begin{pmatrix} N_1^\lambda(t) \\ Z_1^\lambda(t) \end{pmatrix} &= \int d^3r\,\mathrm{g}\left(x'\right)\begin{pmatrix} \dot{x}'\rho_n^\lambda(\vec{r},t) + j_{x,\mathrm{n}}^\lambda(\vec{r},t)\cos\theta + j_{y,\mathrm{n}}^\lambda(\vec{r},t)\sin\theta \\ \dot{x}'\rho_p^\lambda(\vec{r},t) + j_{x,\mathrm{p}}^\lambda(\vec{r},t)\cos\theta + j_{y,\mathrm{p}}^\lambda(\vec{r},t)\sin\theta \end{pmatrix} \\ &= \begin{pmatrix} v_n^\lambda(t) \\ v_p^\lambda(t) \end{pmatrix}. \end{aligned} \tag{3.10}$$

For each $\lambda$ event in the ensemble, the proton current $j_p(\vec{r},t)$ and the neutron current $j_n(\vec{r},t)$ within the window determine the proton drift coefficient $v_p^\lambda(t)$ and the neutron

drift coefficient $v_n^{\lambda}(t)$, respectively. For small values of $\kappa$, instead of using the delta function, we can replace it with a Gaussian distribution $g(x)$. The equation for this substitution is as follows:

$$g(x) = \frac{1}{\kappa\sqrt{2\pi}} \exp\left(-x^2/2\kappa^2\right), \tag{3.11}$$

$\kappa = 1.0$ fm is in the lattice spacing order for numerical computations. The current density vector in the SMF approach is defined as,

$$\begin{aligned}\vec{j}_{\alpha}^{\lambda}(\vec{r},t) &= \frac{\hbar}{2im}\sum_{ij\in\alpha}\left[\Phi_j^{*\alpha}(\vec{r},t;\lambda)\vec{\nabla}\Phi_i^{\alpha}(\vec{r},t;\lambda) - \Phi_i^{\alpha}(\vec{r},t;\lambda)\vec{\nabla}\Phi_j^{*\alpha}(\vec{r},t;\lambda)\right]\rho_{ji}^{\lambda} \\ &= \frac{\hbar}{m}\sum_{ij\in\alpha}\mathrm{Im}\left(\Phi_j^{*\alpha}(\vec{r},t;\lambda)\vec{\nabla}\Phi_i^{\alpha}(\vec{r},t;\lambda)\rho_{ji}^{\lambda}\right).\end{aligned} \tag{3.12}$$

The ensemble average of the Langevin equations is used to calculate the mean proton $Z_1(t) = \overline{Z_1^{\lambda}(t)}$ and neutron $N_1(t) = \overline{N_1^{\lambda}(t)}$ numbers of projectile-like and target-like collision partners. Using the mean values for density matrix elements $\overline{\rho_{ji}^{\lambda}} = \delta_{ji}n_j$ with small fluctuations TDHF equations can be written as,

$$\frac{d}{dt}\begin{pmatrix}N_1(t)\\Z_1(t)\end{pmatrix} = \int d^3r g\left(x'\right)\begin{pmatrix}\dot{x}'\rho_n(\vec{r},t) + \hat{e}\cdot\vec{j}_n(\vec{r},t)\\ \dot{x}'\rho_p(\vec{r},t) + \hat{e}\cdot\dot{j}_p(\vec{r},t)\end{pmatrix} = \begin{pmatrix}v_n(t)\\v_p(t)\end{pmatrix}, \tag{3.13}$$

where mean values of the nucleon density,

$$\rho_{\alpha}(\vec{r},t) = \sum_{h\in\alpha}\Phi_h^{*\alpha}(\vec{r},t)\Phi_h^{\alpha}(\vec{r},t), \tag{3.14}$$

and the current density is defined as,

$$\vec{j}_{\alpha}(\vec{r},t) = \frac{\hbar}{m}\sum_{h\in\alpha}\mathrm{Im}\left(\Phi_h^{*\alpha}(\vec{r},t)\vec{\nabla}\Phi_h^{\alpha}(\vec{r},t)\right). \tag{3.15}$$

The subscript $h$ in equations Eq. 3.14 and Eq. 3.15 denotes the summation over the occupied states of the projectile and target nuclei, which are referred to as "hole"

states. The net currents of protons and neutrons across the window plane are indicated by the drift coefficients $v_n(t)$ and $v_p(t)$. One can linearize the Langevin equation around the mean values of $N_1(t)$ and $Z_1(t)$ to compute the fluctuations around the mean values of neutron and proton numbers. Fluctuations can be caused by two distinct sources. The first source is the variation in wave functions across various events, denoted as $\lambda$. The second source is the initial stochastic fluctuations in the density matrix components, represented as $\delta\rho^{\lambda}_{ji} = \rho^{\lambda}_{ji} - \delta_{ji}n_j$.

In the stochastic Langevin equation, the neutron $v^{\lambda}_n(t)$ and proton $v^{\lambda}_p(t)$ drift coefficients of an ensemble in the event $\lambda$ are determined by the proton and neutron currents in the window; their fluctuations, $\delta v^{\lambda}_n(t)$ and $\delta v^{\lambda}_p(t)$, respectively, are expressed as stochastic expressions of the proton and neutron currents. For small amplitude variations, the drift coefficients $v_n(t)$ and proton $v_p(t)$ are approximated as linear functions around their average values,

$$\begin{pmatrix} \mathrm{v}^{\lambda}_p(t) \\ \mathrm{v}^{\lambda}_n(t) \end{pmatrix} = \begin{pmatrix} \mathrm{v}_p(t) \\ \mathrm{v}_n(t) \end{pmatrix} + \begin{pmatrix} \frac{\partial \mathrm{v}_p}{\partial Z_1}\left(Z^{\lambda}_1 - \overline{Z^{\lambda}_1}\right) + \frac{\partial \mathrm{v}_p}{\partial N_1}\left(N^{\lambda}_1 - \overline{N^{\lambda}_1}\right) \\ \frac{\partial \mathrm{v}_n}{\partial Z_1}\left(Z^{\lambda} - \overline{Z^{\lambda}_1}\right) + \frac{\partial \mathrm{v}_n}{\partial N_1}\left(N^{\lambda}_1 - \overline{N^{\lambda}_1}\right) \end{pmatrix} + \begin{pmatrix} \delta\mathrm{v}^{\lambda}_p(t) \\ \delta\mathrm{v}^{\lambda}_n(t) \end{pmatrix}. \quad (3.16)$$

The stochastic components of the proton and neutron currents give rise to the fluctuations $\delta\mathrm{v}^{\lambda}_p(t)$ and $\delta\mathrm{v}^{\lambda}_n(t)$ in the SMF theory. These fluctuations are uncorrelated Gaussian distributions with mean values of $\overline{\delta\mathrm{v}^{\lambda}_p(t)} = 0$ and $\overline{\delta\mathrm{v}^{\lambda}_n(t)} = 0$. In the Markovian approximation, the variances are related to the diffusion coefficients of proton and neutron exchange, denoted as $D_{ZZ}(t)$ and $D_{NN}(t)$, respectively as,

$$\overline{\delta\mathrm{v}^{\lambda}_p(t)\delta\mathrm{v}^{\lambda}_p\left(t'\right)} = 2\delta\left(t - t'\right) D_{ZZ}(t), \quad (3.17)$$

$$\overline{\delta\mathrm{v}^{\lambda}_n(t)\delta\mathrm{v}^{\lambda}_n\left(t'\right)} = 2\delta\left(t - t'\right) D_{NN}(t), \quad (3.18)$$

and mixed diffusion coefficient is $D_{ZN}(t) = 0$. Using Eq. 3.10, temporal change in fluctuations of neutron and proton numbers written as,

$$\frac{d}{dt}\begin{pmatrix}\delta Z_1^\lambda(t)\\ \delta N_1^\lambda(t)\end{pmatrix} = \begin{pmatrix}\frac{\partial \mathrm{v}_p}{\partial Z_1}\left(Z_1^\lambda - \overline{Z_1^\lambda}\right) + \frac{\partial \mathrm{v}_p}{\partial N_1}\left(N_1^\lambda - \overline{N_1^\lambda}\right)\\ \frac{\partial \mathrm{v}_n}{\partial Z_1}\left(Z^\lambda - \overline{Z_1^\lambda}\right) + \frac{\partial \mathrm{v}_n}{\partial N_1}\left(N_1^\lambda - \overline{N_1^\lambda}\right)\end{pmatrix} + \begin{pmatrix}\delta \mathrm{v}_p^\lambda(t)\\ \delta \mathrm{v}_n^\lambda(t)\end{pmatrix}. \tag{3.19}$$

If the fluctuations are coherent around the average values, the linear limit becomes even more accurate at approximating small amplitude fluctuations. The derivatives of the drift coefficients evolve along the mean trajectory. The following definition of $\delta v_\alpha^\lambda(t)$ gives the stochastic parts of the drift coefficients: $\delta\vec{j}_\alpha^\lambda(\vec{r},t)$ represents the fluctuations in the current density and the elements of the density matrix $\delta\rho_\alpha^\lambda(\vec{r},t)$ as follows,

$$\delta v_\alpha^\lambda(t) = \int d^3r g\left(x'\right)\left(\dot{x}'\delta\rho_\alpha^\lambda(\vec{r},t) + \hat{e}\cdot\delta\vec{j}_\alpha^\lambda(\vec{r},t)\right). \tag{3.20}$$

In the above equation, fluctuations in neutron and proton current density are written as,

$$\delta\vec{j}_\alpha^\lambda(\vec{r},t) = \frac{\hbar}{m}\sum_{ij\in\alpha}\mathrm{Im}\left(\Phi_j^{*\alpha}(\vec{r},t)\vec{\nabla}\Phi_i^\alpha(\vec{r},t)\delta\rho_{ji}^\lambda\right), \tag{3.21}$$

and fluctuations in elements of neutron and proton density matrix,

$$\delta\rho_\alpha^\lambda(\vec{r},t) = \sum_{ij\in\alpha}\Phi_j^{*\alpha}(\vec{r},t)\delta\rho_{ji}^\lambda\Phi_i^\alpha(\vec{r},t). \tag{3.22}$$

### 3.2.2 Dispersion Calculations for Fragment Charge and Mass Distributions

The normal vector $\hat{e}$ to the window plane can be determined in Eq. 3.20. Instead of the Dirac delta function, we employ the Gaussian distribution given in Eq. 3.11 for small values of $\kappa$. For collision partners, neutron, proton, and mixed variances can be defined as follows:

$$\sigma_{NN}^2(t) = \overline{\left(N_1^\lambda - \overline{N_1^\lambda}\right)^2}, \tag{3.23}$$

$$\sigma^2_{ZZ}(t) = \overline{\left(Z_1^\lambda - \overline{Z_1^\lambda}\right)^2}, \tag{3.24}$$

$$\sigma^2_{NZ}(t) = \overline{\left(N_1^\lambda - \overline{N_1^\lambda}\right)\left(Z_1^\lambda - \overline{Z_1^\lambda}\right)}. \tag{3.25}$$

The temporal change of these variances is written as,

$$\frac{\partial}{\partial t}\sigma^2_{NN} = 2\frac{\partial \mathrm{v}_n}{\partial N_1}\sigma^2_{NN} + 2\frac{\partial \mathrm{v}_n}{\partial Z_1}\sigma^2_{NN} + 2D_{NN}, \tag{3.26}$$

$$\frac{\partial}{\partial t}\sigma^2_{ZZ} = 2\frac{\partial \mathrm{v}_p}{\partial Z_1}\sigma^2_{ZZ} + 2\frac{\partial \mathrm{v}_p}{\partial N_1}\sigma^2_{NZ} + 2D_{ZZ}, \tag{3.27}$$

$$\frac{\partial}{\partial t}\sigma^2_{NZ} = \frac{\partial \mathrm{v}_p}{\partial N_1}\sigma^2_{NN} + \frac{\partial \mathrm{v}_n}{\partial Z_1}\sigma^2_{ZZ} + \sigma^2{}_{NZ}\left(\frac{\partial \mathrm{v}_p}{\partial Z_1} + \frac{\partial \mathrm{v}_n}{\partial N_1}\right). \tag{3.28}$$

To calculate variances from Eqns. 3.26, 3.27, 3.28, diffusion coefficients and derivatives of drift coefficients should be known.

### 3.2.3 Derivation of Neutron and Proton Diffusion Coefficients

We mentioned that $\overline{\delta \mathrm{v}_n^\lambda(t)} = 0\, \overline{\delta \mathrm{v}_p^\lambda(t)} = 0$, the fluctuations resulting from the stochastic components of the drift coefficients have zero mean values. The proton and neutron diffusion coefficients are defined by integrating the relevant correlation functions over the time span of the process,

$$\int_0^t dt' \delta \mathrm{v}_\alpha^\lambda(t) \delta \mathrm{v}_\alpha^\lambda(t') = D_{\alpha\alpha}(t). \tag{3.29}$$

Current density fluctuations around the window plane and density fluctuations are the two main sources of the stochastic components of the drift coefficients. The current density changes become more apparent because of the greater nucleon flow rate relative to the window's collective velocity. Consequently, for the stochastic components

of the drift coefficients, the following equation only considers the variations in current density.

$$\delta v_{\alpha}^{\lambda}(t) = \frac{\hbar}{m} \int d^3 r g\left(x'\right) \sum_{ij \in \alpha} \operatorname{Im}\left[\phi_j^* \alpha(\vec{r}, t) \hat{\mathrm{e}} \cdot \vec{\nabla} \phi_i^{\alpha}(\vec{r}, t) \delta \rho_{ji}^{\lambda}\right]. \tag{3.30}$$

In this context, the subscript $j \in P$ represents the summation over the states from which the projectile nucleus originates, while the subscript $i \in T$ represents the summation over the states from which the target nucleus originates. The diffusion coefficient becomes,

$$\begin{aligned} D_{\alpha\alpha}(t) &= \int_0^t dt' \overline{\delta v_{\alpha}^{\lambda}(t) \delta v_{\alpha}^{\lambda}\left(t'\right)} \\ &= \int_0^t dt' \operatorname{Re}\left[\sum_{p \in P,\ \mathrm{h} \in \mathrm{T}} A_{ph}^{\alpha}(t) A_{ph}^{*}\left(t'\right) + \sum_{p \in T,\ \mathrm{h} \in P} A_{ph}^{\alpha}(t) A_{ph}^{*}\left(t'\right)\right]. \end{aligned} \tag{3.31}$$

In Eq. 3.31, $p$ and $h$ subscripts denote particle and hole states, respectively, for collision partners. Matrix elements can be written as,

$$\begin{aligned} A_{ph}^{\alpha}(t) &= \frac{\hbar}{2m} \int d^3 r g\left(x'\right) \left(\Phi_p^{*\alpha}(\vec{r}, t) \hat{e} \cdot \vec{\nabla} \Phi_h^{\alpha}(\vec{r}, t) - \Phi_h^{\alpha}(\vec{r}, t) \hat{e} \cdot \vec{\nabla} \Phi_p^{*\alpha}(\vec{r}, t)\right) \\ &= \frac{\hbar}{m} \int d^3 r g\left(x'\right) \Phi_p^{*\alpha}(\vec{r}, t) \left(\hat{e} \cdot \vec{\nabla} \Phi_h^{\alpha}(\vec{r}, t) - \frac{x'}{2\kappa^2} \Phi_h^{\alpha}(\vec{r}, t)\right). \end{aligned} \tag{3.32}$$

Equation 3.31 includes an infinitive number of particle states; thus, the following approximation is used, if empty states are added and subtracted to the first term of Eq. 3.31,

$$\sum_{p \in P, h \in T} A_{ph}^{\alpha}(t) A_{ph}^{*\alpha}\left(t'\right) = \sum_{a \in P, h \in T} A_{ah}^{\alpha}(t) A_{ah}^{*\alpha}\left(t'\right) - \sum_{h' \in P, h \in T} A_{h'h}^{\alpha}(t) A_{h'h}^{*\alpha}\left(t'\right). \tag{3.33}$$

All of the projectile's states are added up to form the summation. Since the wave functions include distinct times, the first term cannot be eliminated by applying the completeness property of the wave functions. Nevertheless, the single-particle wave functions that vary with time demonstrate a nearly diabatic nature within short intervals.

Thus, during the brief time evolution $\tau = t - t'$, the time-dependent wave functions can be shifted forwards or backwards using the expression $\Phi_a\left(\vec{r}, t'\right) \approx \Phi_a(\vec{r} - \vec{u}\tau, t)$, where $\vec{u}(\vec{R}, T)$ represents the drift velocity of nucleons passing through the window. This velocity depends on the average position $\vec{R} = \left(\vec{r}_1 + \vec{r}_2\right)/2$ and the average time $T = \left(t + t'\right)/2$. Therefore, the completeness relation can be expressed as follows:

$$\sum_a \Phi_a^*\left(\vec{r}_1, t\right) \Phi_a\left(\vec{r}_2 - \vec{u}\tau, t\right) = \delta\left(\vec{r}_1 - \vec{r}_2 + \vec{u}\tau\right), \tag{3.34}$$

and Eq. 3.33 becomes,

$$\sum_{a\in P, h\in T} A_{ah}^{\alpha}(t) A_{ah}^{*\alpha}\left(t'\right) = \sum_{h\in T} \int d^3r_1 d^3r_2 \delta\left(\vec{r}_1 - \vec{r}_2 + \vec{u}_h\tau\right) W_h^{\alpha}\left(\vec{r}_1, t\right) W_h^{*\alpha}\left(\vec{r}_2, t'\right), \tag{3.35}$$

where the hole states simply need to be added up. For every chosen drift velocity, the completeness relation provided by Eq. 3.34 is applicable. For each term in the total, choosing the velocity of the empty states $\vec{u}_h(\vec{R}, T)$ is the best option. Therefore, by eliminating the summation over single-particle states, the calculation of the quantal diffusion coefficients becomes much simplified. One needs to take into account empty states originating from the target ion. The term $W_h^{\alpha}\left(\vec{r}_1, t\right)$ in Eq. 3.35 can be expressed as follows:

$$W_h^{\alpha}\left(\vec{r}_1, t\right) = \frac{\hbar}{m} g\left(x_1'\right) \left(\hat{e} \cdot \vec{\nabla}_1 \Phi_h^{\alpha}\left(\vec{r}_1, t\right) - \frac{x_1'}{2\kappa^2} \Phi_h^{\alpha}\left(\vec{r}_1, t\right)\right). \tag{3.36}$$

Equation 3.35 becomes,

$$\sum_{a\in P, h\in T} A_{ah}^{\alpha}(t) A_{ah}^{*\alpha}\left(t'\right) = \int d^3r \tilde{g}\left(x'\right) G_T(\tau) J_{\perp,\alpha}^T(\vec{r}, t - \tau/2), \tag{3.37}$$

where Appendix B of [43] has the computational details. Here in Eq. 3.37, $J_{\perp,\alpha}^T(\vec{r}, t - \tau/2)$ represents the sum of the magnitudes of the current densities perpendicular to the window for each wave function coming from the target, and its explicit expression is given by,

$$J^{T}_{\perp,\alpha}(\vec{r},t-\tau/2)=\frac{\hbar}{m}\sum_{h\in T}\left|\mathrm{Im}\,\Phi^{*\alpha}_{h}(\vec{r},t-\tau/2)\left(\hat{e}\cdot\vec{\nabla}\Phi^{\alpha}_{h}(\vec{r},t-\tau/2)\right)\right|, \quad (3.38)$$

$G^{h}_{T}(\tau)$ at $\tau$ is the memory kernel defined as,

$$G^{h}_{T}(\tau)=\frac{1}{\sqrt{4\pi}}\frac{1}{\tau^{h}_{T}}\exp\left[-\left(\tau/2\tau^{h}_{T}\right)^{2}\right], \quad (3.39)$$

for the memory time, $\tau^{h}_{T}=\kappa/\left|\vec{u}^{h}_{\perp}\right|$. But we are using an approximation by replacing $G^{h}_{T}(\tau)$ with its average value,

$$G_{T}(\tau)=\frac{1}{\sqrt{4\pi}\tau_{T}}\exp\left[-\left(\tau/2\tau_{T}\right)^{2}\right]. \quad (3.40)$$

A similar analysis can be performed for the second term as well,

$$\sum_{a\in T,h\in P}A^{\alpha}_{ah}(t)A^{*\alpha}_{ah}\left(t'\right)=\int d^{3}r\tilde{g}\left(x'\right)G_{P}(\tau)J^{P}_{\perp,\alpha}(\vec{r},t-\tau/2). \quad (3.41)$$

The total of the average magnitudes of the current densities of the wave functions originating from the projectile ion is represented by $J^{P}_{\perp,\alpha}(\vec{r},t-\tau/2)$ in the equation above. For convenience, the lowercase vector $\vec{r}$ is employed instead of the uppercase letter $R$. The proton and neutron diffusion coefficients can be expressed in the following form,

$$\begin{aligned}D_{\alpha\alpha}(t)=&\int_{0}^{t}d\tau\int d^{3}r\tilde{g}\left(x'\right)\left[G_{T}(\tau)J^{T}_{\perp,\alpha}(\vec{r},t-\tau/2)+G_{P}(\tau)J^{P}_{\perp,\alpha}(\vec{r},t-\tau/2)\right]\\&-\int_{0}^{t}d\tau\,\mathrm{Re}\left[\sum_{h'\in P,\ \mathrm{h}\in\mathrm{T}}A^{\alpha}_{h'h}(t)A^{*'}_{h'h}(t-\tau)+\sum_{h'\in T,\ \mathrm{h}\in P}A^{\alpha}_{h'h}(t)A^{*\alpha}_{h'h}(t-\tau)\right].\end{aligned} \quad (3.42)$$

This expression, derived from a fully quantum mechanical framework and a microscopic form, contains no adjustable parameters. The integral over time in the expression corresponds to memory effects. It automatically includes the Pauli blocking effect, which has no classical counterpart. In this expression, the summation is only

over a finite number of occupied states, and these single-particle wave functions are obtained from TDHF solutions.

### 3.2.4 Calculating the Derivatives of Drift Coefficients

To determine the covariances as described by the Eqns. 3.26, 3.27, 3.28, it is necessary to calculate not only the diffusion coefficients but also the derivatives of the drift coefficients. The one-sided flux method is used to calculate the drift coefficient derivatives. As a side note, when the charge asymmetry values of the colliding ions are equal or nearly equal, the net drift becomes zero, rendering this approach ineffective. If that is the case, neighbouring reaction systems with different charge asymmetry, the same energy in the CM frame, and the same initial angular momentum could be used for calculating the reduced curvature parameters $\alpha$ and $\beta$. While calculating the iso-scalar curvature parameter $\beta$, the selected point's charge asymmetry must be close to the colliding ions and near the iso-scalar drift path. The selected point's charge asymmetry for the iso-vector curvature parameter must be very different from those of the colliding ions and far from the iso-scalar drift path. The calculations will also be at the same energy and initial angular momentum as the central system. In this way, the criteria guarantee proper conditions for the appropriate determination of curvature parameters and the related drift and diffusion coefficients.

In all of the systems studied in this work, initial charge asymmetries of the reaction partners are different, resulting in a distinct mean-drift path shown in Figs. 2.2(a), 2.3(a), 2.4(a), 2.5(a) and 2.6(a). The potential energy surface of the two-center nuclear system governs the diffusion of protons and neutrons in the $N - Z$ plane. Symmetry energy enables rapid diffusion in the direction perpendicular to the average drift path (beta stability valley), resulting in a swift equalization of the charge asymmetry. Meanwhile, the process of diffusion proceeds at a slow pace through the beta stability valley.

The collision partner's state is represented by $N_1, Z_1$ on the $N - Z$ plane in Fig. 3.2, while the system's local equilibrium point is shown by $N_0, Z_0$. When the charge asymmetries of the collision partners are close to the charge asymmetry of the composite system, the quick equilibration of the charge asymmetry is not easily observ-

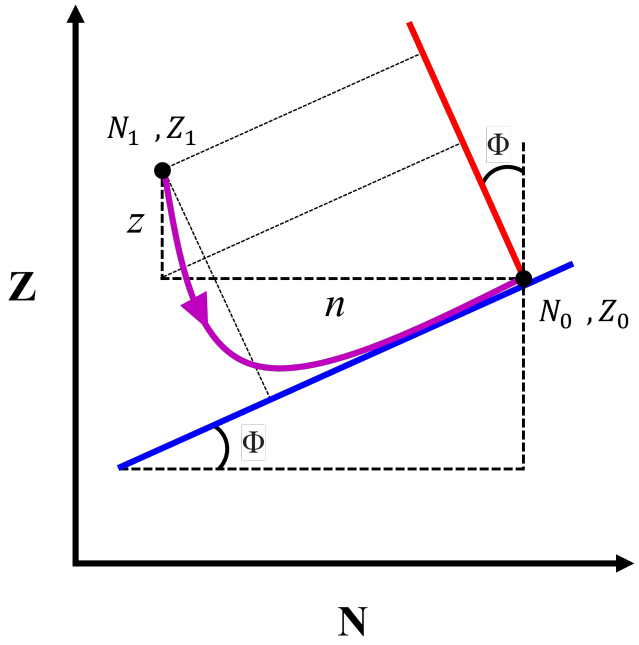


Figure 3.2: Example drift path on the $N - Z$ plane. The solid red line represents the iso-vector drift, and the solid blue line represents the iso-scaler drift. The drift path is illustrated with a solid magenta line. $N_1, Z_1$ is the projectile or target-like fragment and $N_0, Z_0$ is the local equilibrium point.

able. During the extended period of interaction, we notice that the two-center nuclear system gradually moves towards a state of symmetry. However, it eventually separates before achieving complete symmetry. From this insight, it is feasible to parameterize the potential energy surface of the two-center nuclear system for each collision parameter, using $N_1$ and $Z_1$ as variables, in the following manner:

$$U\left(N_1, Z_1\right) = \frac{1}{2}b(n\cos\phi - z\sin\phi)^2 + \frac{1}{2}a(n\sin\phi + z\cos\phi)^2. \tag{3.43}$$

The equation consists of two terms. The first term represents the iso-vector drift path perpendicular to the beta-stability valley line. The second term represents the iso-scalar drift path along the beta-stability valley line. Here, $n = N_0 - N_1$ and $z = Z_0 - Z_1$ as shown on the Fig. 3.2. For any point $N_1, Z_1$, the distance from the iso-vector path is represented by the term $n\cos\phi - z\sin\phi$, and the distance from the iso-scalar path is represented by the term $n\sin\phi + z\cos\phi$. The Einstein relation,

which explains the relationship between the diffusion and drift coefficients in the transport mechanism of collective variables, is utilized to find the reduced curvature parameters $\alpha$ and $\beta$. The Einstein relation states that the relationship between the neutron drift coefficient $v_n(t)$ and the proton drift coefficient $v_p(t)$, as well as their respective diffusion coefficients, could be expressed as follows:

$$\begin{aligned} v_n(t) &= -\frac{D_{NN}}{T}\frac{\partial U}{\partial N_1} \\ &= D_{NN}\left(\beta R_v(t)\cos\phi + \alpha R_S(t)\sin\phi\right), \end{aligned} \tag{3.44}$$

$$\begin{aligned} v_p(t) &= -\frac{D_{ZZ}}{T}\frac{\partial U}{\partial Z_1} \\ &= D_{ZZ}\left(\beta R_v(t)\sin\phi - \alpha R_s(t)\cos\phi\right). \end{aligned} \tag{3.45}$$

The relationship between the temperature and the curvature parameters can be expressed as $\beta = b/T$ and $\alpha = a/T$. The terms $R_v(t) = n\cos\phi - z\sin\phi$ and $R_S(t) = n\sin\phi + z\cos\phi$ represent the orthogonal distances of the collision partner, defined by $N_1$ and $Z_1$, from the iso-scalar and iso-vector paths, respectively. Therefore, the derivatives of the drift coefficients with respect to the diffusion coefficients and curvature parameters can be determined in the following manner:

$$\frac{\partial v_n(t)}{\partial N_1} = -D_{NN}\left(\beta\cos^2\phi + \alpha\sin^2\phi\right), \tag{3.46}$$

$$\frac{\partial v_n(t)}{\partial Z_1} = +D_{NN}(\alpha-\beta)\cos\phi\sin\phi, \tag{3.47}$$

$$\frac{\partial v_p(t)}{\partial Z_1} = -D_{ZZ}\left(\beta\sin^2\phi + \alpha\cos^2\phi\right), \tag{3.48}$$

$$\frac{\partial v_p(t)}{\partial N_1} = +D_{ZZ}(\alpha-\beta)\cos\phi\sin\phi. \tag{3.49}$$

These expressions relate the derivatives of the drift coefficients to the diffusion coefficients and the curvature parameters, incorporating the angle $\phi$ between the beta stability valley and the neutron number axis.

The time-dependent reduced curvature parameters are influenced by shell effects and the microscopic character of the collision dynamics included in TDHF. In a macroscopic transport description, one has to average out this time dependence. Consequently, we calculate the reduced curvature parameters by taking the average over an appropriate time span. As observed from the drift path depicted in Figs. 2.2(a), 2.3(a), 2.4(a), 2.5(a), and 2.6(a), the drift occurs in the direction of symmetry. Points labeled as A and B along the drift path are utilized to compute the mean value of the iso-vector reduced curvature parameter. The B to C proportion is utilized to compute the mean value of the iso-scalar reduced curvature parameter. Corresponding times of these points are shown in Figs. 2.2(b), 2.3(b), 2.4(b), 2.5(b) and 2.6(b).

The time interval between the initial contact point for the collision partners at $t_A$ to the point where the charge asymmetry equilibrium is reached, the point $t_B$, is chosen to compute the average iso-vector reduced curvature parameter. During this time frame, the average value of the iso-vector reduced curvature parameter is determined as:

$$\alpha = \frac{1}{R_S} \int_{t_A}^{t_B} \left\{ \frac{v_n(t) \sin\phi}{D_{NN}(t)} - \frac{v_p(t) \cos\phi}{D_{ZZ}(t)} \right\} dt. \tag{3.50}$$

Taking the average on the same time interval, we can calculate iso-vector distance as,

$$\begin{aligned} R_S = \int_{t_A}^{t_B} \{ & [N_1(t) - N_0] \sin\phi \\ & - [Z_1(t) - Z_0] \cos\phi \} \, dt. \end{aligned} \tag{3.51}$$

The average value of the iso-scalar reduced curvature parameter for the time interval from $t_B$ to $t_C$, when the collision partners are close to separation, is determined as:

$$\beta = -\frac{1}{R_V} \int_{t_B}^{t_C} \left\{ \frac{v_n(t) \cos\phi}{D_{NN}(t)} + \frac{v_p(t) \sin\phi}{D_{ZZ}(t)} \right\} dt. \tag{3.52}$$

The iso-scalar distance can be found by taking the average on the same time interval,

$$\begin{aligned} R_V = \int_{t_B}^{t_C} \{ & [N_1(t) - N_0] \cos\phi \\ & + [Z_1(t) - Z_0] \sin\phi \} \, dt. \end{aligned} \tag{3.53}$$

For the $^{64}$Ni + $^{130}$Te and $^{206}$Pb + $^{118}$Sn reaction systems, in numerical calculations, the perpendicular $R_S$ and $R_V$ distances fluctuate abruptly, yielding unrealistic results for the reduced curvature parameters. To address this issue, we included perpendicular distance to the integral term to smooth out the fluctuations in the selected time intervals. For these systems the $\alpha$ reduced curvature parameter becomes,

$$\alpha = \frac{1}{t_B - t_A} \int_{t_A}^{t_B} \left( \frac{v_n(t) \sin\phi}{D_{NN}} - \frac{v_p(t) \cos\phi}{D_{ZZ}} \right) / R_s(t) dt, \tag{3.54}$$

and the $\beta$ reduced curvature parameter becomes,

$$\beta = \frac{1}{t_C - t_B} \int_{t_B}^{t_C} \left( \frac{v_n(t) \cos\phi}{D_{NN}} + \frac{v_p(t) \sin\phi}{D_{ZZ}} \right) / R_v(t) dt \tag{3.55}$$

### 3.3 Results of TDHF + SMF Calculations for Selected Heavy-Ion Systems

To calculate diffusion coefficients, reduced curvature parameters and the dispersions, the following initial angular momenta were utilized for reaction systems: $^{58}$Fe+$^{208}$Pb at $\ell = 40\hbar$, $^{36}$S + $^{238}$U at $\ell = 40\hbar$, $^{64}$Ni + $^{130}$Te at $\ell = 82\hbar$ and $^{206}$Pb + $^{118}$Sn at $\ell = 60\hbar$. These initial angular momenta were selected to maximize the drift before the collision partners separated, making the mean drift path of the reaction system more pronounced.

Diffusion coefficients for the reaction systems were calculated using Eq. 3.42, and the results shown in Figs. 3.3(a), 3.4(a), 3.5(a), 3.6(a), 3.7(a). The solid blue line depicts the time variation of the neutron diffusion coefficient, whereas the dashed red line indicates the variation of the proton diffusion coefficient. The data shows that the neutron diffusion coefficients are approximately double the value of the proton diffusion coefficients. The observed effect is anticipated as a result of the repulsive force between protons, known as Coulomb repulsion, and the fact that the colliding partners are nuclei with an excess of neutrons [44, 42, 43, 45, 46, 47, 48, 27, 49, 50, 51, 52, 53, 54].

The reaction system's potential energy surface is described by the reduced curvature parameters $\alpha$ and $\beta$, whose average values are calculated through the time intervals

Table 3.1: Calculated average curvature parameters and their time intervals in $^{58}$Fe + $^{208}$Pb reaction with $E_{\text{c.m.}} = 238.5$ MeV, $^{36}$S + $^{238}$U reaction with $E_{\text{c.m.}} = 151.1$ MeV, $^{64}$Ni + $^{130}$Te reaction with $E_{\text{c.m.}} = 184.3$ MeV and $^{206}$Pb + $^{118}$Sn reaction with $E_{\text{c.m.}} = 436.8$ MeV. The time intervals between $t_A$ and $t_B$ are utilized for calculating the iso-vector curvature parameter $\alpha$. Similarly, the time intervals between $t_B$ and $t_C$ are employed for calculating the iso-scalar curvature parameter $\beta$ using equations Eq. 3.50 and Eq. 3.52 respectively.

| System | Orientation | $t_A(fm/c)$ | $t_B(fm/c)$ | $t_C(fm/c)$ | $\alpha$ | $\beta(10^{-3})$ |
|---|---|---|---|---|---|---|
| $^{58}$Fe + $^{208}$Pb | tip | 290 | 410 | 1200 | 0.335 | 1.5 |
| | side | 290 | 410 | 1500 | 0.378 | 1.3 |
| $^{36}$S + $^{238}$U | - | 350 | 550 | 3500 | 0.245 | 11.1 |
| $^{64}$Ni + $^{130}$Te | - | 270 | 500 | 2200 | 0.269 | 8.0 |
| $^{206}$Pb + $^{118}$Sn | - | 270 | 400 | 800 | 0.542 | 7.0 |

$t_A$, $t_B$, and $t_C$. These points correspond to the locations labelled as $A$, $B$, and $C$ on the mean drift paths displayed in Figs. 2.2(a), 2.3(a), 2.4(a), 2.5(a), 2.6(a) using Eqs. 3.50 and 3.52. Table 3.1 shows the average values of the reduced curvature parameters determined by the calculations and the corresponding time intervals.

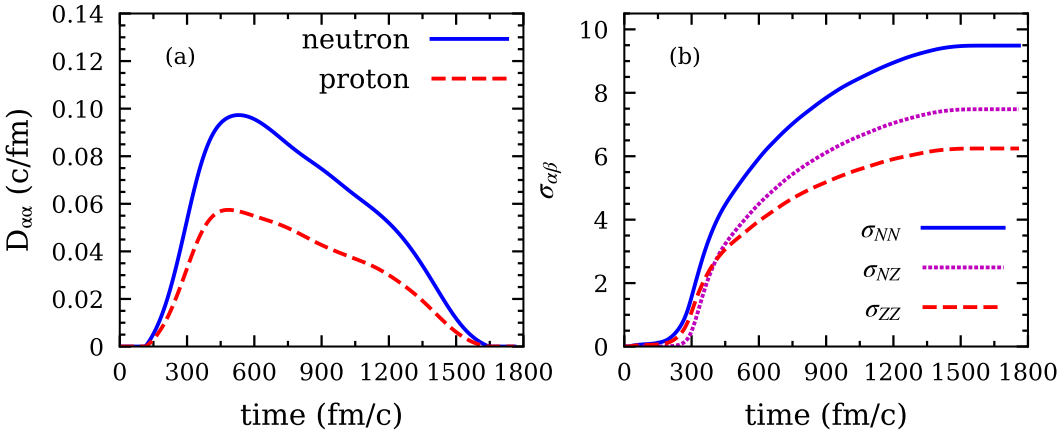


Figure 3.3: Calculated (a) neutron and proton diffusion coefficients, (b) neutron, proton and mixed dispersions of the $^{58}$Fe + $^{208}$Pb at $E_{\text{c.m.}} = 238.5$ MeV for the tip orientation of the $^{58}$Fe nucleus with an initial angular momentum of $\ell = 40\hbar$.

Solutions to the coupled differential Eqns. 3.26, 3.27 and 3.28 yield the neutron, pro-

ton and mixed dispersions. These equations are solved with the initial conditions, $\sigma^2_{NN}(t=0)=0$, $\sigma^2_{ZZ}(t=0)=0$ and $\sigma^2_{NZ}(t=0)=0$ for each system with the selected initial angular momentum range. For the $^{58}$Fe + $^{208}$Pb system at $\ell = 40\hbar$, temporal change of the neutron, proton and mixed variances shown in Fig. 3.3(b) for the tip orientation and in Fig. 3.4(b) for the side orientation with a solid blue line, red dashed line and dotted magenta line respectively. Results of the calculations for each initial angular momentum for this system are given in Table 3.2 for the tip orientation and Table 3.3 for the side orientation.

Table 3.2: SMF results for the $^{58}$Fe + $^{208}$Pb reaction at $E_{\text{c.m.}} = 238.5$ MeV in the tip orientation of the $^{58}$Fe nucleus with an initial angular momentum of $\ell = 40\hbar$.

| $\ell_i$ | $\sigma_{NN}$ | $\sigma_{ZZ}$ | $\sigma_{NZ}$ | $\sigma_{AA}$ |
|---|---|---|---|---|
| 40 | 9.5 | 6.2 | 7.5 | 15.5 |
| 60 | 7.8 | 5.1 | 6.0 | 12.6 |
| 80 | 4.5 | 3.0 | 3.2 | 7.1 |
| 100 | 1.5 | 0.8 | 0.4 | 1.8 |
| 120 | 0.8 | 0.5 | 0.1 | 1.0 |
| 140 | 0.6 | 0.3 | 0.1 | 0.7 |
| 160 | 0.4 | 0.2 | 0.0 | 0.5 |
| 180 | 0.3 | 0.1 | 0.0 | 0.3 |
| 200 | 0.2 | 0.1 | 0.0 | 0.2 |
| 220 | 0.2 | 0.1 | 0.0 | 0.2 |
| 240 | 0.1 | 0.0 | 0.0 | 0.1 |

For $^{58}$Fe + $^{208}$Pb system in the tip orientation with an initial angular momentum of $\ell = 40\hbar$, as shown in Fig. 3.3, from the beginning of the interaction up to $t \approx$450 fm/c, dispersion has the following order of magnitudes $\sigma_{NZ} < \sigma_{ZZ} < \sigma_{NN}$. As the nucleon exchange continues, correlation develops between the exchange partners and after $t \approx$ fm/c point, this ordering changes to $\sigma_{ZZ} < \sigma_{NZ} < \sigma_{NN}$ showing that after substantial energy dissipation, correlations become important. Within the standard mean-field framework, magnitudes of fluctuations and the correlation is underestimated in the dissipative collisions, and correlation term $\sigma_{NZ}$ is calculated as zero. In the SMF approach, these fluctuations are much larger, yielding a more realistic picture. Similar

behaviour on variances is also observed for the rest of the systems studied in this work. As nucleon exchange slows at around $t \approx 1500$ fm/c, dispersions reach the final asymptotic values.

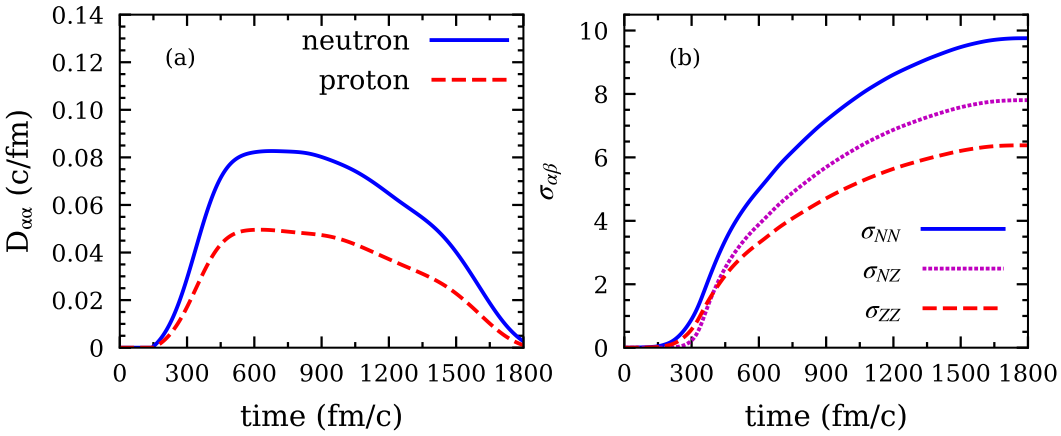


Figure 3.4: Calculated (a) neutron and proton diffusion coefficients, (b) neutron, proton and mixed dispersions of the $^{58}$Fe + $^{208}$Pb reaction with $E_{\text{c.m.}} = 238.5$ MeV for the side orientation of the $^{58}$Fe nucleus with an initial angular momentum of $\ell = 40\hbar$.

Table 3.3: SMF results of the $^{58}$Fe + $^{208}$Pb reaction with $E_{\text{c.m.}} = 238.5$ MeV for the side orientation of the $^{58}$Fe nucleus with an initial angular momentum $\ell = 40\hbar$.

| $\ell_i$ | $\sigma_{NN}$ | $\sigma_{ZZ}$ | $\sigma_{NZ}$ | $\sigma_{AA}$ |
|---|---|---|---|---|
| 40 | 9.2 | 6.0 | 7.2 | 15.0 |
| 60 | 4.4 | 3.0 | 3.2 | 7.0 |
| 80 | 2.2 | 1.4 | 1.0 | 3.0 |
| 100 | 1.1 | 0.6 | 0.2 | 1.3 |
| 120 | 0.8 | 0.4 | 0.1 | 0.9 |
| 140 | 0.6 | 0.1 | 0.1 | 0.7 |
| 160 | 0.4 | 0.2 | 0.0 | 0.5 |
| 180 | 0.3 | 0.2 | 0.0 | 0.4 |
| 200 | 0.2 | 0.1 | 0.0 | 0.3 |
| 220 | 0.2 | 0.1 | 0.0 | 0.2 |
| 240 | 0.1 | 0.1 | 0.0 | 0.1 |

In Fig. 3.4, neutron, proton, and mixed dispersions are displayed in side orientation

of the $^{58}$Fe + $^{208}$Pb system for $\ell = 40\hbar$. Similar to the tip orientation of the same system, dispersion exhibits the following order of magnitudes from the beginning of the contact until approximately $t \approx 450$ fm/c. The ordering of $\sigma_{NZ}$, $\sigma_{ZZ}$, and $\sigma_{NN}$ changes as correlation becomes important. Initially, $\sigma_{NZ}$ is less than $\sigma_{ZZ}$, which is less than $\sigma_{NN}$. However, as correlation becomes more significant, the ordering changes to $\sigma_{ZZ}$ being less than $\sigma_{NZ}$, which is less than $\sigma_{NN}$. This transition occurs when the system reaches asymptotic values at around $t \approx 1500$ fm/c.

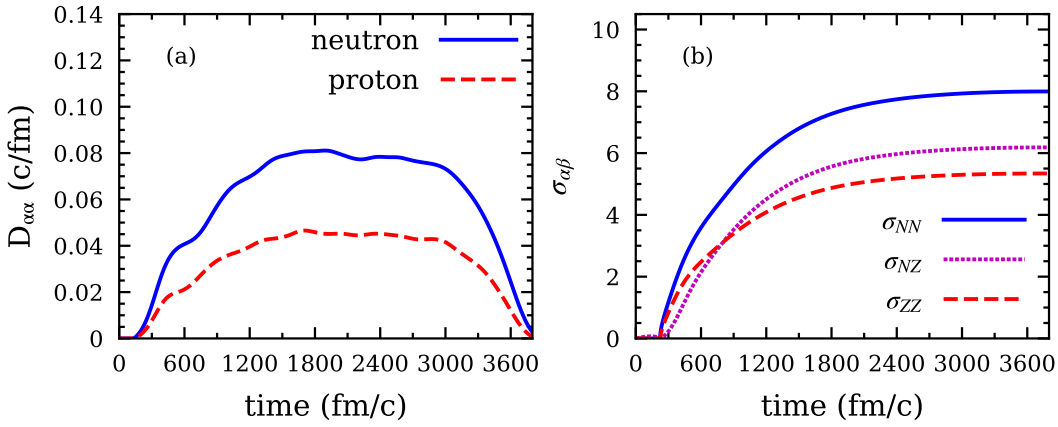


Figure 3.5: Calculated (a) neutron and proton diffusion coefficients, (b) neutron, proton and mixed dispersions of the $^{36}$S + $^{238}$U reaction at $E_{\text{c.m.}} = 151.1$ MeV with an initial angular momentum of $\ell = 40\hbar$.

For the $^{36}$S + $^{238}$U system with an initial angular momentum of $\ell = 40\hbar$, calculated dispersions presented on Fig. 3.5(b). Around $t \approx 800$ fm/c, correlation develops and order of magnitude changes as $\sigma_{ZZ} < \sigma_{NZ} < \sigma_{NN}$. Beyond the $t \approx 3300$ fm/c point, nucleon exchange slows down, and dispersions reach their asymptotic values.

On Fig. 3.6(b), calculated dispersions presented for the $^{64}$Ni + $^{130}$Te reaction system with an initial angular momentum of $\ell = 82.\hbar$. Beyond $t \approx 600$ fm/c, correlations becomes effective and order of magnitude changes to $\sigma_{ZZ} < \sigma_{NZ} < \sigma_{NN}$. After $t \approx 2750$ fm/c, dispersions arrive at their asymptotic values as the nucleon exchange slows down.

For $^{206}$Pb + $^{118}$Sn system with an initial angular momentum of $\ell = 60\hbar$, results of the dispersion calculations presented on the Fig. 3.7(b). Correlations become significant after $t \approx 400$ fm/c, and as nucleon exchange decelerates beyond $t \approx 700$ fm/c, the

Table 3.4: SMF results of the $^{36}$S + $^{238}$U reaction with $E_{\text{c.m.}} = 151.1$ MeV with an initial angular momentum of $\ell = 40\hbar$.

| $\ell_i$ | $\sigma_{NN}$ | $\sigma_{ZZ}$ | $\sigma_{NZ}$ | $\sigma_{AA}$ |
|---|---|---|---|---|
| 34 | 7.9 | 5.3 | 6.1 | 12.9 |
| 35 | 7.9 | 5.2 | 6.1 | 12.8 |
| 36 | 7.8 | 5.2 | 6.0 | 12.7 |
| 37 | 7.9 | 5.3 | 6.1 | 12.8 |
| 38 | 8.0 | 5.3 | 6.2 | 13.0 |
| 39 | 8.0 | 5.4 | 6.2 | 13.1 |
| 40 | 8.0 | 5.3 | 6.2 | 13.0 |
| 41 | 4.3 | 2.9 | 2.8 | 6.5 |
| 42 | 3.6 | 2.4 | 2.1 | 5.3 |
| 44 | 3.0 | 2.1 | 1.5 | 4.3 |
| 46 | 2.5 | 1.7 | 1.1 | 3.4 |
| 48 | 1.9 | 1.2 | 0.5 | 2.3 |
| 50 | 1.4 | 0.9 | 0.3 | 1.8 |

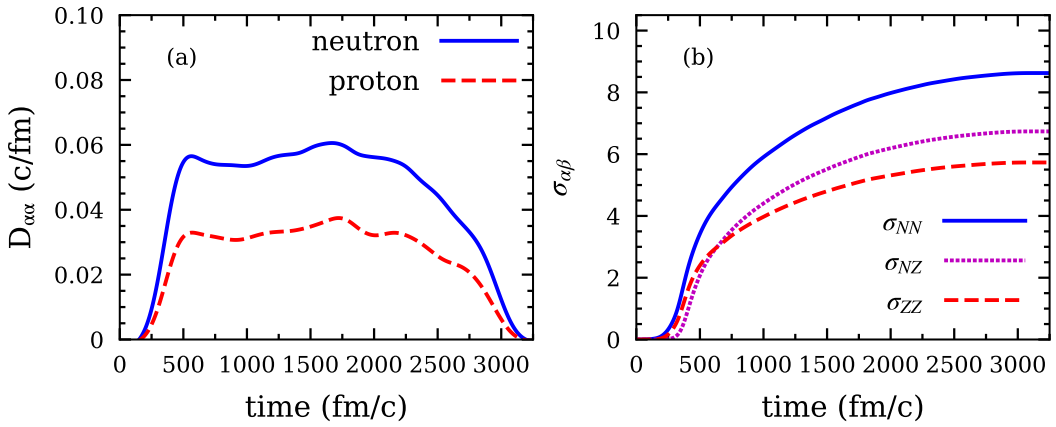


Figure 3.6: Calculated (a) neutron and proton diffusion coefficients, (b) neutron, proton and mixed dispersions of the $^{64}$Ni + $^{130}$Te reaction at $E_{\text{c.m.}} = 184.3$ MeV with an initial angular momentum of $\ell = 82\hbar$.

dispersions reach their asymptotic values.

Table 3.5: SMF results of the $^{64}$Ni + $^{130}$Te reaction with $E_{\text{c.m.}} = 184.3$ MeV with an initial angular momentum of $\ell = 82\hbar$.

| $\ell_i$ | $\sigma_{NN}$ | $\sigma_{ZZ}$ | $\sigma_{NZ}$ | $\sigma_{AA}$ |
|---|---|---|---|---|
| 82 | 8.6 | 5.7 | 6.7 | 14.1 |
| 84 | 4.2 | 2.9 | 2.8 | 6.4 |
| 86 | 3.9 | 2.6 | 2.5 | 5.9 |
| 88 | 2.8 | 1.9 | 1.4 | 4.0 |
| 90 | 2.6 | 1.7 | 1.2 | 3.5 |
| 92 | 2.0 | 1.2 | 0.6 | 2.5 |
| 94 | 1.7 | 0.9 | 0.4 | 2.0 |
| 96 | 1.5 | 0.8 | 0.3 | 1.7 |
| 98 | 1.3 | 0.7 | 0.2 | 1.5 |
| 100 | 1.2 | 0.7 | 0.2 | 1.5 |
| 110 | 0.9 | 0.5 | 0.1 | 1.0 |
| 120 | 0.7 | 0.4 | 0.1 | 0.8 |
| 140 | 0.4 | 0.2 | 0.0 | 0.5 |
| 160 | 0.3 | 0.1 | 0.0 | 0.3 |
| 180 | 0.2 | 0.1 | 0.0 | 0.2 |

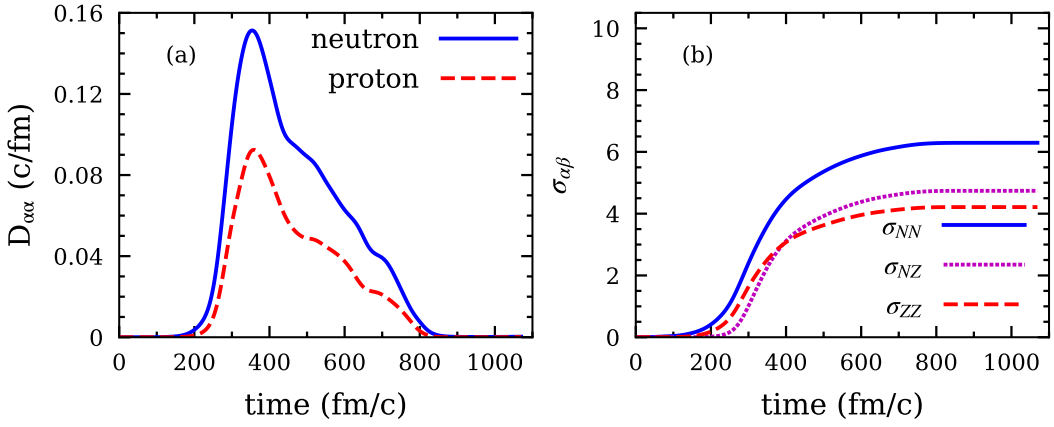


Figure 3.7: Calculated (a) neutron and proton diffusion coefficients, (b) neutron, proton and mixed dispersions of the $^{206}$Pb + $^{118}$Sn reaction with $E_{\text{c.m.}} = 436.8$ MeV with an initial angular momentum of $\ell = 60\hbar$.

Table 3.6: SMF results of the $^{206}$Pb + $^{118}$Sn reaction with $E_{\text{c.m.}} = 436.8$ MeV with an initial angular momentum of $\ell = 60\hbar$.

| $\ell_i$ | $\sigma_{NN}$ | $\sigma_{ZZ}$ | $\sigma_{NZ}$ | $\sigma_{AA}$ |
|---|---|---|---|---|
| 60 | 6.3 | 4.2 | 4.8 | 10.2 |
| 80 | 6.1 | 4.1 | 4.6 | 9.8 |
| 100 | 5.7 | 3.9 | 4.3 | 9.2 |
| 120 | 5.2 | 3.5 | 3.8 | 8.3 |
| 140 | 4.6 | 3.1 | 3.2 | 7.2 |
| 160 | 3.7 | 2.5 | 2.4 | 5.6 |
| 180 | 2.7 | 1.8 | 1.4 | 3.8 |
| 200 | 1.7 | 0.9 | 0.4 | 2.0 |
| 220 | 1.2 | 0.6 | 0.2 | 1.4 |
| 240 | 1.0 | 0.5 | 0.1 | 1.1 |
| 260 | 0.8 | 0.4 | 0.1 | 0.9 |

$$\sigma^2_{AA}(\ell) = \sigma^2_{NN}(\ell) + \sigma^2_{ZZ}(\ell) + 2\sigma^2_{NZ}(\ell). \tag{3.56}$$

Using the dispersions calculated in this section, mass variance can be calculated as in Eq. 3.56. The next chapter will present calculation details for the production yield and cross-sections of primary and secondary fragments. Subsequently, the results obtained from these calculations for the reaction systems studied in this work will be compared with the available experimental data.

# CHAPTER 4

# FRAGMENT DISTRIBUTION AND CROSS-SECTION CALCULATIONS

## 4.1 Probability Distribution Calculations for the Production of Primary Fragments

The solutions of a Langevin equation, Eq. 3.19, obtained in numerous iterations, define the joint probability distribution function $P_\ell(N, Z)$ for creation of binary fragments with $N$ neutrons and $Z$ protons. For the distribution function of macroscopic variables, the Langevin equation is similar to the Fokker-Planck equation [55]. In this specific case, where the drifts are linear functions of macroscopic variables as described by Eq. 3.19, the distribution function for protons and neutrons at the initial orbital angular momentum $\ell$ can be expressed using a correlated Gaussian distribution. This distribution is characterized by the mean values and dispersions for neutrons, protons, and their mixed dispersions.

$$P_\ell(N, Z) = \frac{1}{2\pi\sigma_{NN}(\ell)\sigma_{ZZ}(\ell)\sqrt{1-\rho_\ell^2}} \exp\left(-C_\ell\right), \tag{4.1}$$

$C_\ell$ exponent for initial angular momentum $\ell$ defined as,

$$\begin{aligned} C_\ell =& \frac{1}{2\left(1-\rho_\ell^2\right)} \left[ \left(\frac{Z-Z_\ell}{\sigma_{ZZ}(\ell)}\right)^2 - 2\rho_\ell \left(\frac{Z-Z_\ell}{\sigma_{ZZ}(\ell)}\right)\left(\frac{N-N_\ell}{\sigma_{NN}(\ell)}\right) \right. \\ & \left. + \left(\frac{N-N_\ell}{\sigma_{NN}(\ell)}\right)^2 \right]. \end{aligned} \tag{4.2}$$

In the above equation, the correlation coefficient is defined as,

$$\rho_\ell = \frac{\sigma^2_{NZ}(\ell)}{[\sigma_{ZZ}(\ell)\sigma_{NN}(\ell)]}. \tag{4.3}$$

The mean neutron and proton numbers for projectile-like and target-like fragments, as obtained from the TDHF computations, are denoted by the symbols $N_\ell$ and $Z_\ell$. The double probabilities can be determined by substituting the expression for the cross-section with the mass number distribution. The summation is performed across $N$ and $Z$ while maintaining a constant total mass number $A = N + Z$ within the probability distribution of the resulting fragment's mass numbers.

$$P^S_l(A) = \frac{1}{\sqrt{2\pi}} \frac{1}{\sigma^S_{AA}(l)} \exp\left[-\frac{1}{2}\left(\frac{A - A^S_l}{\sigma^S_{AA}(l)}\right)^2\right], \tag{4.4}$$

where mass variance $\sigma_{AA}$ defined by the Eq. 3.56. Here, the $S$ superscript defines the fragment type as projectile-like or target-like.

## 4.2 Cross-Section Calculations for Primary Products

To calculate the cross-section for the primary products of the reaction, we can utilize the standard expression as [56],

$$\sigma^S(N, Z) = \frac{\pi\hbar^2}{2\mu E_{c.m}} \sum_{l_{\min}}^{l_{\max}} (2l + 1) P^S_l(N, Z), \tag{4.5}$$

where $\mu$ is the reduced mass of the reaction system. $P^S_l(N, Z)$ defined as,

$$P^S_l(N, Z) = \frac{1}{2}\left[P^S_{l,pro}(N, Z) + P^S_{l,\mathrm{tar}}(N, Z)\right]. \tag{4.6}$$

To ensure the total probability distribution is normalized to unity, the $1/2$ factor is added to the above equation. The cross-section for the mass distribution is similarly written as,

$$\sigma^{s}(A) = \frac{\pi\hbar^2}{2\mu E_{\text{c.m.}}} \sum_{\ell_{\min}}^{\ell_{\max}} (2\ell+1) P_{\ell}^{s}(A), \tag{4.7}$$

where $P_l^S(A)$ defined as,

$$P_l^S(A) = \frac{1}{2}\left[P_{l,pro}^S(A) + P_{l,\text{tar}}^S(A)\right]. \tag{4.8}$$

The production yield of the primary fragments can be calculated in a manner similar to that used for the cross-section expression as follows,

$$Y(A) = \frac{1}{\sum_{\ell_{\min}}^{\ell_{\max}}(2\ell+1)} \sum_{\ell_{\min}}^{\ell_{\max}} (2\ell+1) P_{\ell}(A). \tag{4.9}$$

Experimental investigations for the reaction system studied in this work [20, 21, 22] show that for the mass symmetric region between the QF peaks, fusion-fission (FF) reaction mechanism has great contribution which cannot be calculated using TDHF. To gain insight into the fragment distribution of that region, statistical decay code GEMINI++ is utilized [52]. Using this methodology, within the mass asymmetric region, the compound nucleus excitation energy is calculated as,

$$E_{CN}^{*} = E_{\text{c.m.}} + Q_{\text{gg}}, \tag{4.10}$$

where $Q_{gg}$ is the disintegration energy released in the fusion reaction. Distribution of the primary fragments becomes,

$$Y(A)^{sum} = \eta_1 Y^{QF}(A) + \eta_2 Y^{FF}(A), \tag{4.11}$$

here, $\eta_1$ is the normalization factor for the QF region, and $\eta_2$ is the normalization factor for the FF region. $\eta_1$ is calculated by fitting the calculated QF data to the experimental data in the QF region. Similarly, the $\eta_2$ is calculated by fitting the calculated FF data to the FF region of the experimental data.

### 4.3 Cross-Section Calculations for Secondary Products

Initially excited, primary fragments cool down by fission or releasing light particles like protons, neutrons, and alpha particles. To incorporate these de-excitation processes into the primary product computations, we utilize the GEMINI++ toolkit, a C++ library containing statistical functions for de-excitation [57]. The following expression is utilized to estimate the overall excitation energy of the generated primary fragments,

$$E^*_\ell(Z,N) = E_{\text{c.m.}} - \text{TKE}_\ell - Q_{\text{gg}}(Z,N). \tag{4.12}$$

In the above equation, $TKE$ represents the final value of the total kinetic energy in collisions with the initial orbital angular momentum $\ell$, and $Q_{gg}(Z,N)$ indicates the ground state $Q$ value of the resulting primary fragments compared to the initial value. Collisions involving an initial orbital angular momentum $\ell$ will result in distributions of the total spin and excitation energy in the exit channel centerd around their average values. This approach does not consider the variations in excitation energy and spin of the primary fragments. We distribute the average value of the total excitation energy and total angular momentum transfer according to the mass ratio of the primary fragments. The parent nucleus, which is in an excited state, releases particles and performs secondary fissions until it can no longer decay due to insufficient energy. The GEMINI++ toolkit calculates the probability $W\left(N,Z \rightarrow N',Z'\right)$ of transitioning from an excited parent nucleus with proton and neutron numbers $(Z,N)$, excitation energy $E^*(Z,N)$, and spin $J$ to the final nucleus $Z',N'$.

The probability distribution of secondary fragments is given by,

$$P^{\text{sec}}_\ell\left(N',Z'\right) = \sum_{N \geqslant N'} \sum_{Z \geqslant Z'} P^{\text{pri}}_\ell\left(N,Z\right) W\left(N,Z \rightarrow N',Z'\right), \tag{4.13}$$

the summation over $Z$ and $N$ includes all pairs of projectile-like and target-like fragments of the di-nuclear system according to their probability distributions. The cross-section for the secondary fragments, $\sigma^{\text{sec}}_\ell(N',Z')$ is then expressed as,

$$\sigma_{\ell}^{\mathrm{sec}}\left(N', Z'\right) = \frac{\pi\hbar^2}{2\mu E_{\mathrm{c.m.}}} \sum_{\ell_{\mathrm{min}}}^{\ell_{\mathrm{max}}} (2\ell+1) P_{\ell}^{\mathrm{sec}}\left(N', Z'\right), \tag{4.14}$$

where the summation over $\ell$ ranges from $\ell_{min}$ to $\ell_{max}$.

## 4.4 Calculation Results for Selected Heavy-Ion Systems and Comparison with Experiments

As previously discussed in the TDHF results section (see Section 2.4), the range of initial angular momentum for the studied system spans from the point where QF is observed to the point where the reaction becomes purely elastic. We divide this initial angular momentum range into smaller intervals to optimize computing time while preserving the details of reaction dynamics at different impact parameters.

Further refinement may be required to improve comparability before matching our results with the available experimental data. For experiments measuring the final fragment scattering angles, which can be compared to our calculations, we compute our cross-sections within the initial angular momentum range corresponding to the experimentally observed scattering angles of the final reaction products in the laboratory frame.

For the $^{58}$Fe + $^{208}$Pb reaction with $E_{\mathrm{c.m.}} = 238.5$ MeV, within the initial angular momentum range of $40\hbar \leq \ell \leq 240\hbar$, the scattering angles of the final fragments are calculated as $50.1^{\circ} \leq \theta_1^{lab} \leq 86.7^{\circ}$ and $35.7^{\circ} \leq \theta_2^{lab} \leq 58.8^{\circ}$ for tip orientation, and $50.6^{\circ} \leq \theta_1^{lab} \leq 81.1^{\circ}$ and $38.8^{\circ} \leq \theta_2^{lab} \leq 58.4^{\circ}$ for side orientation, as presented in Table 2.1. In the experimental data for this system, final reaction products are measured with the CORSET spectrometer [20], with measurement arms placed at $\theta_1^{lab} = 60 \pm 20$ degrees and $\theta_2^{lab} = 60 \pm 20$ degrees, which are covered by our calculations. Therefore, the initial angular momentum range $40\hbar \leq \ell \leq 240\hbar$ is also used in calculations for final product yields and cross-sections.

Similarly, an initial angular momentum range of $60\hbar \leq \ell \leq 260\hbar$ is considered for the $^{206}$Pb + $^{118}$Sn reaction with $E_{\mathrm{c.m.}} = 436.8$ MeV. Table 2.4 displays the computed scattering angles in the laboratory frame, which correspond to the angular coverage

range of the experiment. The detector was positioned at $\theta_{lab} = 25°$ [22].

In the $^{64}$Ni + $^{130}$Te reaction with $E_{\text{c.m.}} = 184.3$ MeV, an initial angular momentum range of $82\hbar \leq \ell \leq 180\hbar$ is considered, and the calculated scattering angles of the final fragments are presented in Table 2.3. In this case, no angular measurements of the scattered final products were made in the experiment [21]. Thus, we utilized the same initial angular momentum range for final product calculations.

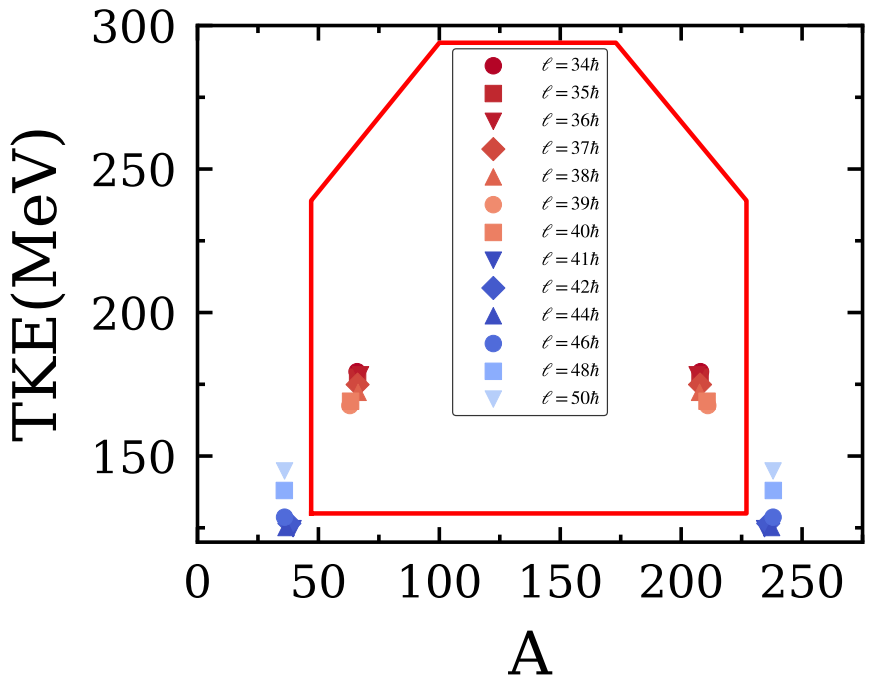


Figure 4.1: Selection of initial angular momentum for production yield calculations of $^{36}$S + $^{238}$U reaction with $E_{\text{c.m.}} = 151.1$ MeV. Corresponding $\ell$ values for $TKE$ points that reside inside the red selection box [20] are utilized for yield calculations.

In the experiment for the $^{36}$S + $^{238}$U reaction with $E_{\text{c.m.}} = 151.1$ MeV [20], a selection box was applied on the $TKE - A$ plane to eliminate contributions from elastic events for yield calculations. Measurements outside this selection box were considered elastic events due to the higher $TKE$ of the fragments. We employed a similar methodology for this system to enhance compatibility with the experimental data. Using the TDHF calculations presented in Table 2.2, we plotted the $TKE$ of the final fragments for each initial angular momentum against their final masses. Figure 4.1 illustrates the $TKE$ points corresponding to the final masses with different initial angular momenta. The selection box used in the experiment was also plotted, and points

outside this box were considered elastic and excluded from the production yield calculations. Based on these results, the initial angular momentum range $34\hbar \leq \ell \leq 40\hbar$ was considered for the yield calculations of final reaction products.

For the $^{58}$Fe+$^{208}$Pb and $^{36}$S+$^{238}$U reaction systems, experimental data are available in the form of mass distributions of primary fragment yields [20]. For the $^{64}$Ni + $^{130}$Te system, experimental data include secondary production cross-sections for various transfer channels and mass distributions of secondary products [21]. For the $^{206}$Pb + $^{118}$Sn system, experimental data are available for secondary production cross-sections across different transfer channels [22].

Figure 4.2 shows the primary cross-sections for the final reaction product. The white stars indicate the highest cross-section points. Peak points for $^{58}$Fe + $^{208}$Pb, $^{64}$Ni + $^{130}$Te and $^{206}$Pb + $^{118}$Sn systems corresponds to the initial projectile and target pairs with zero nucleon exchange, meaning that the quasi-elastic and elastic reaction dominate around the peak points. For $^{36}$S + $^{238}$U system, as we mentioned before, we excluded most of the contributions from the elastic reactions to comply with the experiment. As we can see from Fig. 4.2(b), this results in a broader peak, where the lighter peak is located at $Z = 27, N = 39$ and heavier peak located at $Z = 81, N = 127$ with relatively lower peak cross-section compared to the other systems.

Figure 4.3 shows the SMF results for the QF process and the GEMINI++ results for the FF process according to the MNT mechanism. The dashed light-blue lines represent the mass distributions of the final primary products estimated using the SMF framework. The orange hatching area indicates the contributions from the FF events, which were computed using the GEMINI++ toolkit. The black dotted lines correspond to the summation obtained using Eq. 4.11. To understand the possible potential surface of these systems, we utilized the proximity model to compute the driving potential of the composite systems. The calculations were conducted using the default settings provided on the NRV site [58], with the distance between mass centers determined via TDHF calculations. Each system's driving potential energy distribution is displayed in the upper panels of Fig. 4.3.

QF and FF processes overlap in the mass-symmetric area, situated between the QF peaks shown in Fig.4.3. The only areas with QF contributions are the mass-asymmetric

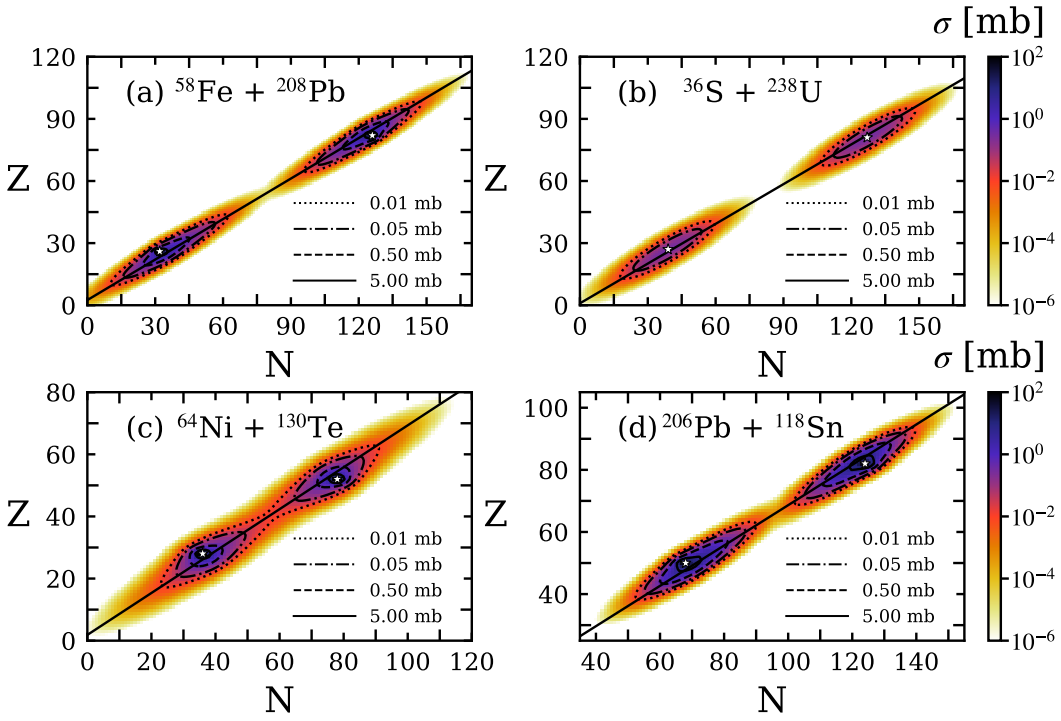


Figure 4.2: Final primary production cross-sections for projectile-like and target-like fragments on the N-Z plane, (a) for the $^{58}$Fe + $^{208}$Pb with $E_{\text{c.m.}} = 238.5$ MeV, (b) for the $^{36}$S + $^{238}$U with $E_{\text{c.m.}} = 151.1$ MeV, (c) for the $^{64}$Ni + $^{130}$Te with $E_{\text{c.m.}} = 184.3$ MeV and (d) for the $^{206}$Pb + $^{118}$Sn with $E_{\text{c.m.}} = 436.8$ MeV. Cross-sections are shown on a logarithmic scale in the units of millibarn.

areas surrounding the initial masses. Using Eq. 4.4, we calculate the probability distributions $P(A)$ for the projectile-like and target-like fragments $A$ in the QF reactions of $^{58}$Fe + $^{208}$Pb in both tip and side geometries. These distributions provide information about the mean mass numbers and mass dispersions for each initial angular momentum value. The contributions from the tip and side collision geometries are combined simply using $P(A) = (P_{tip}(A) + P_{side}(A))/2$.

We assume that the reaction partners are fused and evaporated according to their excitation energies for the FF calculations since we are only interested in observing the shape of the distribution. The computed distributions are compared with the empirical yields indicated by the solid red dots. The normalization constants $\eta_1$ and $\eta_2$ for the QF and FF processes are obtained independently by fitting the experimental yield data at appropriate locations. The experimental peak value is utilized for the $^{36}$S + $^{238}$U

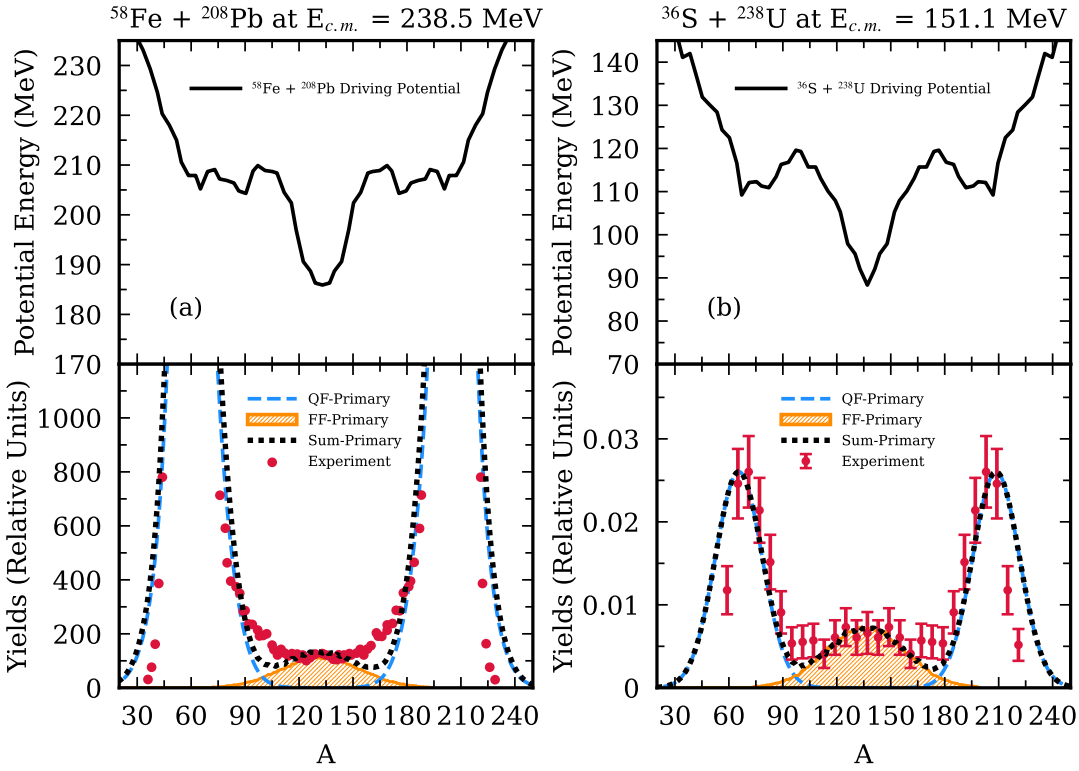


Figure 4.3: Results of the primary fragment yield calculations (bottom) and potential energy surface at the contact point of collision partners (top) for the (a) $^{58}$Fe + $^{208}$Pb reaction with $E_{\text{c.m.}} = 238.5$ MeV and for the (b) $^{36}$S + $^{238}$U reaction with $E_{\text{c.m.}} = 151.1$ MeV. Experimental data obtained from [59] for the $^{58}$Fe+$^{208}$Pb system and [20] for the $^{36}$S + $^{238}$U system.

reaction system. Unfortunately, it is difficult to determine the maximum values in the QF data for the $^{58}$Fe + $^{208}$Pb reaction system. The normalization constant for this reaction system is obtained by utilizing data points near $A = 80$.

The calculations accurately depict how the QF and FF processes depend on the entrance-channel characteristics of the reactions for the systems depicted in Fig.4.3. In the $^{36}$S + $^{238}$U reaction system, due to a smaller Coulomb effect and larger mass asymmetry, a greater number of nucleon exchanges occur. This effect is explained as with an increasing Coulomb factor, the contact time between reaction partners decreases exponentially, meaning a smaller time frame to exchange nucleons [60]. At energies above the Coulomb barrier, the major contribution comes from the FF processes that yield the mass symmetric fragments for $^{36}$S + $^{238}$U system. However, the domi-

nant process for $^{58}$Fe + $^{208}$Pb is the QF process [20]. This is also observed with the Coulomb factors $Z_1Z_2$ presented in Table 4.1.

Up to seven nucleons can be transferred in collisions with low initial angular momentum in the $^{58}$Fe + $^{208}$Pb reaction system, according to TDHF calculations displayed in Tables 2.1 and 2.2. With an increase in the initial angular momentum, the collisions approach a state of near-perfect elasticity, leading to no transfer of nucleons and negligible dispersion of mass. The computed primary mass distribution, as shown in Fig. 4.3(a), exhibits a peak location that is centered around $^{208}$Pb for heavier fragments and $^{58}$Fe for lighter fragments. The SMF approach yields satisfactory outcomes in describing this system's observed distribution of primary fragment masses. However, the data near the mass symmetric region is still underestimated.

The differences can be attributed to the symmetrical distribution of secondary fission fragments as projected by the GEMINI++ toolkit. Shell effects can cause secondary fission to show an uneven mass distribution at low excitation energy of about 0.5 MeV; these effects are not considered by the GEMINI++ toolkit. The limitations of the current diffusion description in SMF theory could also contribute. This is because, at small initial angular momentum values near the fusion formation region, it may be difficult to determine the window position between collision partners, which leads to an underestimate of the diffusion coefficients during the time interval following maximum overlap.

The difference in diffusion coefficients is clearly shown in Figs 3.3(a), 3.4(a), whereas the diffusion behavior for the $^{36}$S + $^{238}$U system in Fig. 3.5 is almost symmetrical. A lower yield around mass symmetry could result from this imbalance in diffusion coefficients. The GEMINI++ toolkit exhibits symmetrical behaviour in its calculations of thermal fission and does not include the influence of shell effects, which become significant at energy levels of about 0.5 MeV. The observed asymmetrical behaviour inside the symmetrical portion of the mass distribution is most likely caused by shell effects.

The impact of the closed shell near the doubly magic $^{208}$Pb nucleus on the $^{36}$S + $^{238}$U reaction system may be noticed by examining the final proton and mass numbers of the target-like fragments $(Z_{f2}, A_{f2})$, as presented in Table 2.3. The duration of con-

tact is enough for the target-like fragments to reach the doubly magic stable $^{208}$Pb nuclei, with an initial angular momentum of $\ell = 40\hbar$ or less. The impact of this phenomenon is also evident in Fig. 4.3(b), where the final primary mass calculations of this system do not consider elastic events. Within the quantal diffusion mechanism framework, a wide range of binary fragments are associated with each initial angular momentum. This complicates precisely determining the experimental angular coverage range in TDHF calculations.

In Fig. 4.3(b), the dotted black line shows yield calculations by summing over the initial angular momentum range $\ell = 34\hbar - 40\hbar$. The primary mass distribution exhibits a peak position close to $A \approx 208$ for target-like fragments. The half-width of the asymmetric QF distribution is 20u, which is calculated as the difference between the mass with the maximum yield and the more symmetric mass with half the maximum yield. This statement is consistent with the findings in Figure 15(a) of reference [59]. The ratio of the integrated yield value within the mass symmetric interval $\frac{A_{CN}}{2} \pm 20$ $(117 \leq A \leq 157)$ to the integrated yield value confined by the bounds of the existing experimental data set $(59 \leq A \leq 221)$ is determined to be $15.2\%$. The observed connection closely matches the calculated ratio of $14.9\%$ obtained from the existing experimental data [20].

There is a strong correlation between the maxima of the mass distribution and the local minima of the potential energy surface [60]. In particular, the lowest potential energy is associated with the highest production of asymmetric QF fragments. The characteristics of asymmetric QF are mostly influenced by the potential energy of the combined system. The maximum yield in the $^{58}$Fe + $^{208}$Pb reaction is found for fragments having masses of around 208u. Nevertheless, the inability to determine the yield peak points makes it impossible to provide a precise value [59]. This correlation additionally emphasizes the role of shell effects in shifting the heavier mass asymmetric peak.

In Fig. 4.4, we show the secondary production cross-sections for $Ni$-like and $Te$-like fragments in the $^{64}$Ni+$^{130}$Te reaction with $E_{\text{c.m.}} = 184.3$ MeV and in Fig. 4.5, for $Sn$-like fragments in the $^{206}$Pb + $^{118}$Sn reaction with $E_{\text{c.m.}} = 436.8$ MeV. The experimental cross-sections are represented by solid red circles, while the secondary production

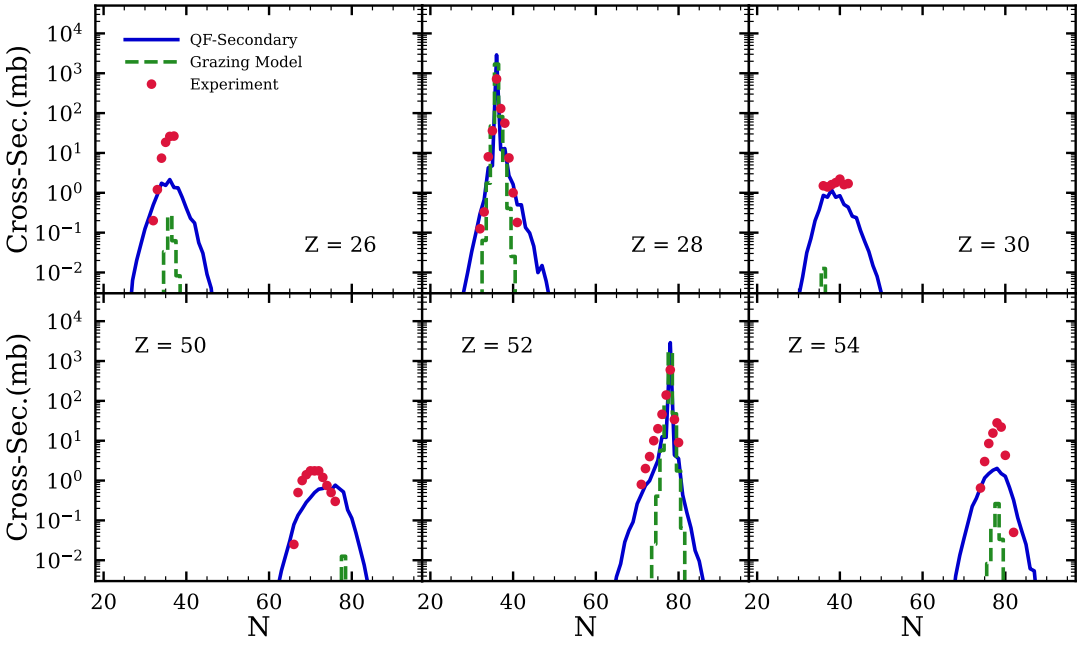


Figure 4.4: Results of the secondary cross-section calculations for $Ni$-like fragments with Z = 26, 28, 30 and for $Te$-like fragments with Z = 50, 52, 54 in the $^{64}$Ni + $^{130}$Te reaction with $E_{\text{c.m.}} = 184.3$ MeV. Results of the GRAZING model [61, 62] were also presented for the same transfer channels. Experimental data obtained from [21].

cross-sections, calculated using the SMF theory, in addition to post-evaporation utilizing the GEMINI++ toolkit, are depicted as solid blue lines. Each panel displays the isotopic distribution of the reaction result based on the neutron number.

The calculated cross-sections for the $^{64}$Ni and $^{130}$Te transfer channels from (-2p) to (+2p) with $E_{\text{c.m.}} = 184.3$ MeV compared with the experimental data [21] in Fig. 4.4. The calculations indicate a tendency to underestimate the experimental results for proton transfer channels of larger amounts, which is also found in other models [63]. In addition, we compare our findings with those of the GRAZING model [61], which is represented by a dashed green line.

The cross-sections for the transfer channels from (+1p) to (-2p) in the $^{206}$Pb + $^{118}$Sn reaction system, with $E_{\text{c.m.}} = 436.8$ MeV, were calculated and compared with experimental data [22]. These calculations were done for the lighter fragments, and the incident energy was above the Bass barrier ($V_{\text{bass}} = 410MeV$). The peak positions and cross-sections exhibit a strong similarity to the experimental results. A review

has been done in a recent study [64] to analyze this reaction within the framework of time-dependent covariant density functional theory.

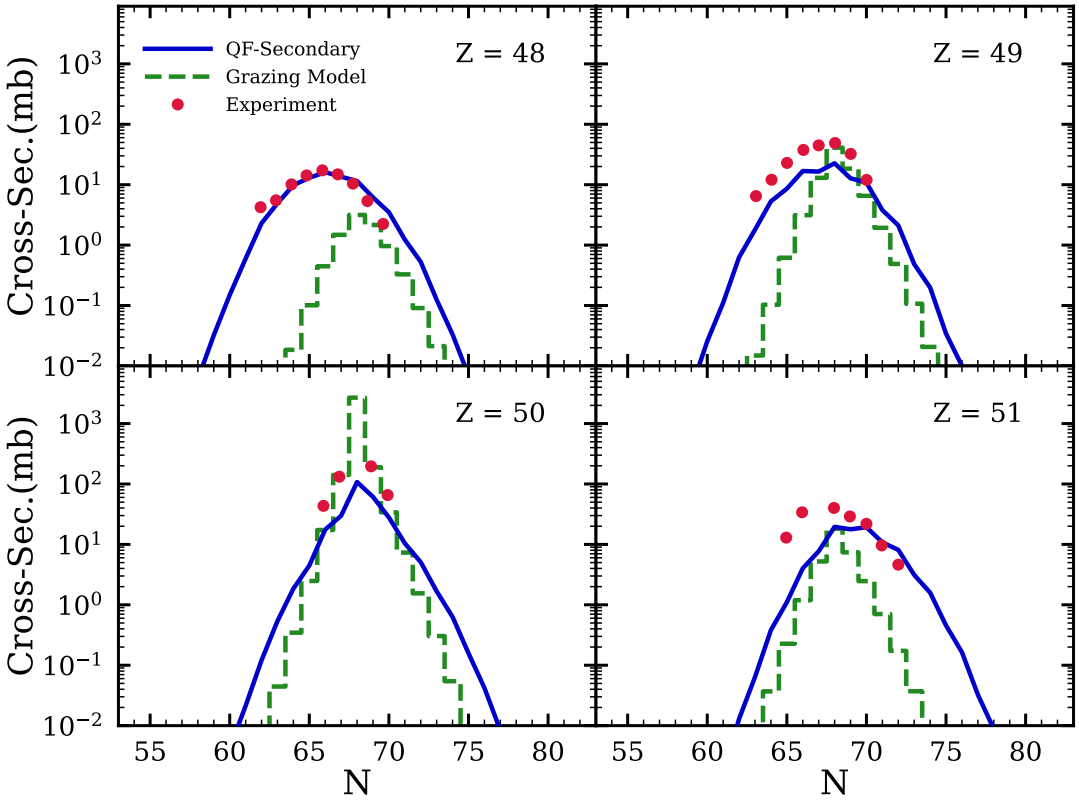


Figure 4.5: Results of the secondary cross-section calculations for $Sn$-like fragments for different transfer channels (Z = 48, 49, 50, 51) in the $^{206}$Pb + $^{118}$Sn reaction with $E_{\text{c.m.}} = 436.8$ MeV. Results of the GRAZING model [61] were also presented for the same transfer channels. Experimental data obtained from [22].

In the bottom portion of Fig. 4.6, the mass distribution of secondary products in the $^{64}$Ni + $^{130}$Te and $^{206}$Pb + $^{118}$Sn systems are presented while corresponding potential energy surface shown at the top. The solid blue line represents the results of the secondary production cross-section calculations based on the SMF approach, with post-evaporation calculations done by the GEMINI++ toolkit. The dashed lighter blue line shows the primary production cross-sections for these systems. For $^{64}$Ni + $^{130}$Te system, experimental mass distribution for secondary products were available [21].

The orange hatches in the symmetric region indicate the contributions from the FF reactions computed using the GEMINI++ toolkit. The dotted black line shows the

summation using a similar equation to Eq. 4.11. In this case, the QF fragments are computed as cross-sections rather than yields; therefore, there is no need for a normalizing factor. As previously done, the FF yields are adjusted to match the experimental data at around $A = 100$.

The secondary fragment distribution of the reaction products in the $^{206}$Pb + $^{118}$Sn system is displayed in Figure 4.6(b). This system does not exhibit FF in this reaction, and no experimental data are available. The dashed line of a lighter blue colour represents the distribution of primary production cross-sections.

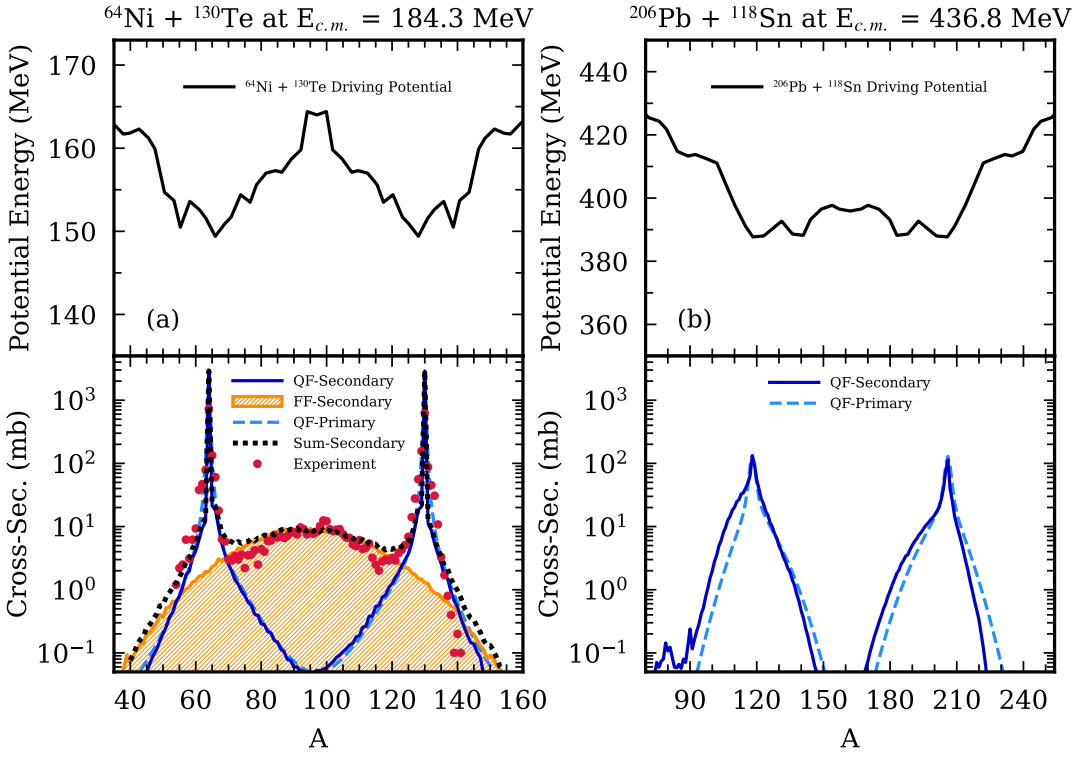


Figure 4.6: Results of the secondary fragment cross-section calculations (bottom) and potential energy surface at the contact point of collision partners (top) for the (a) $^{64}$Ni + $^{130}$Te reaction with $E_{\text{c.m.}} = 184.3$ MeV and for the (b) $^{206}$Pb + $^{118}$Sn reaction with $E_{\text{c.m.}} = 436.8$ MeV. Primary fragment cross-sections are also presented. Experimental data for mass distribution for the $^{64}$Ni + $^{130}$Te system obtained from [21].

In both systems shown in Fig. 4.6, the peak points of the primary and secondary production cross-sections overlap, indicating that most contributions arise from quasi-elastic and elastic reactions near the peak points. In these reactions, the system's

energy is predominantly released as the kinetic energy of the outgoing fragments, resulting in no internal excitation and, therefore, no decay. As we move away from the peaks, contributions from QF reactions increase, suggesting that primary products are more likely to be left excited. The primary and secondary production cross-sections in this region do not completely overlap.

In Fig. 4.6(b), this effect is more noticeable for the $^{206}$Pb + $^{118}$Sn system. The secondary fragments are represented by the blue line in the mass distribution. We find that secondary fission occurs in the highly excited $Pb$-like fragments. The peak observed at $A = 80$ corresponds to the decay products produced due to this fission process. Additionally, the cross-sectional peaks match the local minima on the potential surface depicted in the upper portion of Fig. 4.6.

Table 4.1: Entrance channel parameters, magicity, Coulomb factor, mass asymmetry and positions of the projectile-like and target-like peaks related to exchanged nucleon numbers in the final primary mass distributions of asymmetric QF fragments in reactions.

| Reaction | Magicity | $Z_1Z_2$ | $\eta$ | $M_L$ | $M_H$ | Exc. Nucl. |
|---|---|---|---|---|---|---|
| $^{206}$Pb + $^{118}$Sn | 2 | 4100 | 0.271 | 123 | 201 | 35 |
| $^{58}$Fe + $^{208}$Pb | 2 | 2132 | 0.564 | 65 | 201 | 7 |
| $^{36}$S + $^{238}$U | 1 | 1472 | 0.737 | 67 | 207 | 31 |
| $^{64}$Ni + $^{130}$Te | 1 | 1456 | 0.340 | 68 | 126 | 4 |

Table 4.1 provides each system's reaction results and entrance channel parameters. The table presents the values of the entrance channel charge product ($Z_1Z_2$) and mass asymmetry ($\eta$). $M_L$ and $M_H$ denote the mean mass numbers of the light and heavy fragments at their initial angular momenta when the maximum number of nucleons are exchanged between the reaction partners.

# CHAPTER 5

# SUMMARY AND CONCLUSION

## 5.1 Summary

This thesis presents an in-depth exploration of nuclear reactions, focusing on the application of the quantal diffusion approach based on the SMF theory to low-energy heavy-ion collisions. The study begins with a detailed review of the TDHF theory, discussing its theoretical aspects and relevance to nuclear reaction systems. The TDHF framework, combined with the Skyrme effective interaction, sets the foundation for understanding the initial dynamics of heavy-ion collisions.

The study extends the TDHF solutions stochastically in subsequent chapters using the SMF approach. This extension is crucial as it introduces fluctuations and correlations that are not captured by the mean-field alone. The derivation of the SMF theory is briefly examined, along with the computation of dispersions, which plays a crucial role in describing the MNT processes.

Extensive calculations were performed for selected heavy-ion systems, including $^{58}$Fe + $^{208}$Pb reaction with $E_{\text{c.m.}} = 238.5$ MeV, $^{36}$S + $^{238}$U reaction with $E_{\text{c.m.}} = 151.1$ MeV, $^{64}$Ni + $^{130}$Te reaction with $E_{\text{c.m.}} = 184.3$ MeV and $^{206}$Pb + $^{118}$Sn reaction with $E_{\text{c.m.}} = 436.8$ MeV. These calculations focused on determining the final production cross-sections and yields of primary and secondary fragments resulting from the collisions. The SMF approach, utilizing quantal nucleon diffusion derived from MNT, incorporates the full geometry of collision dynamics without additional adjustable parameters apart from the Skyrme parameters of the TDHF. The statistical code GEMINI++ was employed for evaporation calculations to determine the secondary fragment distributions. The GEMINI++ toolkit is also utilized to calcu-

late contributions from fusion-fission-like events. Understanding the MNT mechanism is crucial for synthesizing neutron-rich super-heavy elements and producing new neutron-rich nuclei.

## 5.2 Conclusion

In conclusion, this thesis demonstrates the usefulness of the quantal diffusion approach based on SMF approach in modelling the dynamics of low-energy heavy-ion collisions. The integration of TDHF and SMF theories offers a comprehensive framework that captures both the deterministic and stochastic aspects of nuclear reactions. The results from this study align well with experimental observations, validating the theoretical models used.

Despite significant advancements in the microscopic description of low-energy heavy-ion reactions using the SMF theory compared to the mean-field models, there are still areas for improvement. The current model linearizes the Langevin equation around the mean trajectory, assuming small amplitude fluctuations, and uses a simple parabolic form for the driving potential $U(N, Z)$; introducing anharmonicity could reduce isotopic width and improve agreement with experimental data. Additionally, the SMF theory has not yet addressed fluctuations in scattering angles and total kinetic energy (TKE) distributions, which are linked to the total excitation energy distribution. Adapting the SMF concept to the relative motion of colliding systems could allow for evaluating TKE fluctuations based on microscopic mean-field dynamics. The SMF theory assumes Gaussian initial fluctuations in the density matrix, which simplifies the formulation of the quantal diffusion approach, but relaxing this assumption could improve the description of higher moments of one-body observables [65, 66]. However, it would require generating a vast ensemble of TDHF trajectories, leading to significant computational costs. Recent proposals, such as applying the SMF concept to the time-dependent reduced density matrix approach, suggest potential extensions of the current framework [67]. These efforts aim to enhance the accuracy of the SMF theory in describing complex nuclear reactions, marking substantial progress in understanding heavy-ion reactions while highlighting the need for further research to refine and expand the theoretical model.

The application of the TDHF-SMF approach to various heavy-ion systems demonstrates its versatility and robustness. The methodologies and findings presented in this thesis pave the way for future research, offering a valuable tool for studying and predicting the outcomes of heavy-ion collisions.

# REFERENCES


[1] Cédric Simenel. Nuclear quantum many-body dynamics. *Eur. Phys. J. A*, 48:152, 2012.

[2] Tea Mijatović. Multinucleon transfer reactions: a mini-review of recent advances. *Frontiers in Physics*, 10:965198, 2022.

[3] Anwar Kamal. *Nuclear Reactions*, pages 425–502. Springer Berlin Heidelberg, Berlin, Heidelberg, 2014.

[4] Alexandre Obertelli and Hiroyuki Sagawa. *Nuclear Shells*, pages 337–370. Springer Singapore, Singapore, 2021.

[5] M Thoennessen. Current status and future potential of nuclide discoveries. *Reports on Progress in Physics*, 76(5):056301, apr 2013.

[6] G. G. Adamian, N. V. Antonenko, A. Diaz-Torres, and S. Heinz. How to extend the chart of nuclides? *Eur. Phys. J. A*, 56:47, 2020.

[7] A. S. Umar, V. E. Oberacker, and C. Simenel. Fusion and quasifission dynamics in the reactions $^{48}\mathrm{Ca} + ^{249}\mathrm{Bk}$ and $^{50}\mathrm{Ti} + ^{249}\mathrm{Bk}$ using a time-dependent Hartree-Fock approach. *Phys. Rev. C*, 94:024605, 2016.

[8] Kazuyuki Sekizawa and Kazuhiro Yabana. Time-dependent Hartree-Fock calculations for multinucleon transfer and quasifission processes in the $^{64}\mathrm{Ni} + ^{238}\mathrm{U}$ reaction. *Phys. Rev. C*, 93:054616, 2016.

[9] Kazuyuki Sekizawa. TDHF Theory and Its Extensions for the Multinucleon Transfer Reaction: A Mini Review. *Front. Phys.*, 7:20, 2019.

[10] C. Simenel and A. S. Umar. Heavy-ion collisions and fission dynamics with the time–dependent Hartree-Fock theory and its extensions. *Prog. Part. Nucl. Phys.*, 103:19–66, 2018.

[11] P. A. M. Dirac. Note on Exchange Phenomena in the Thomas Atom. *Math. Proc. Camb. Phil. Soc.*, 26:376, 1930.

[12] P. Bonche, S. Koonin, and J. W. Negele. One-dimensional nuclear dynamics in time-dependent Hartree-Fock approximation. *Phys. Rev. C*, 13:1226–1258, 1976.

[13] A. S. Umar and V. E. Oberacker. Three-dimensional unrestricted time-dependent Hartree-Fock fusion calculations using the full Skyrme interaction. *Phys. Rev. C*, 73:054607, 2006.

[14] Kazuyuki Sekizawa. *Multinucleon Transfer Reactions and Quasifission Processes in Time-Dependent Hartree-Fock Theory*. PhD thesis, University of Tsukuba, 2015.

[15] Kirsten Vo-Phuoc. *Microscopic Approach to Heavy-Ion Reactions*. PhD thesis, The Australian National University, 2018.

[16] Emma Betty Suckling. *Nuclear structure and dynamics from the fully unrestricted Skyrme-Hartree-Fock model*. PhD thesis, 2011.

[17] T. H. R. Skyrme. CVII. The nuclear surface. *Phil. Mag.*, 1:1043–1054, 1956.

[18] A. S. Umar, M. R. Strayer, J. S. Wu, D. J. Dean, and M. C. Güçlü. Nuclear Hartree-Fock calculations with splines. *Phys. Rev. C*, 44:2512–2521, 1991.

[19] Ka–Hae Kim, Takaharu Otsuka, and Paul Bonche. Three-dimensional TDHF calculations for reactions of unstable nuclei. *J. Phys. G: Nucl. Part. Phys.*, 23:1267, 1997.

[20] I. M. Itkis, E. M. Kozulin, M. G. Itkis, G. N. Knyazheva, A. A. Bogachev, E. V. Chernysheva, L. Krupa, Yu. Ts. Oganessian, V. I. Zagrebaev, A. Ya. Rusanov, F. Goennenwein, O. Dorvaux, L. Stuttgé, F. Hanappe, E. Vardaci, and E. de Goés Brennand. Fission and quasifission modes in heavy-ion-induced reactions leading to the formation of Hs$^*$. *Phys. Rev. C*, 83:064613, 2011.

[21] W. Królas, R. Broda, B. Fornal, T. Pawłat, J. Wrzesiński, D. Bazzacco, G. de Angelis, S. Lunardi, R. Menegazzo, D.R. Napoli, and C. Rossi Alvarez. Dynamical deformation of nuclei in deep-inelastic collisions: A gamma coinci-

dence study of $^{130}$Te+275 MeV $^{64}$Ni and $^{208}$Pb+345 MeV $^{58}$Ni heavy ion reactions. *Nucl. Phys. A*, 832:170–197, 2010.

[22] J. Diklić, S. Szilner, L. Corradi, T. Mijatović, G. Pollarolo, P. Čolović, G. Colucci, E. Fioretto, F. Galtarossa, A. Goasduff, A. Gottardo, J. Grebosz, A. Illana, G. Jaworski, M. Jurado Gomez, T. Marchi, D. Mengoni, G. Montagnoli, D. Nurkić, M. Siciliano, N. Soić, A. M. Stefanini, D. Testov, J. J. Valiente-Dobón, and N. Vukman. Transfer reactions in $^{206}\mathrm{Pb} + ^{118}\mathrm{Sn}$: From quasielastic to deep-inelastic processes. *Phys. Rev. C*, 107:014619, 2023.

[23] K. Nishio, H. Ikezoe, S. Mitsuoka, I. Nishinaka, Y. Nagame, Y. Watanabe, T. Ohtsuki, K. Hirose, and S. Hofmann. Effects of nuclear orientation on the mass distribution of fission fragments in the reaction of $^{36}\mathrm{S} + ^{238}\mathrm{U}$. *Phys. Rev. C*, 77:064607, 2008.

[24] S. Ayik. A stochastic mean-field approach for nuclear dynamics. *Phys. Lett. B*, 658:174, 2008.

[25] Kazuyuki Sekizawa. Microscopic description of production cross sections including deexcitation effects. *Phys. Rev. C*, 96:014615, 2017.

[26] Cédric Simenel. Particle Transfer Reactions with the Time-Dependent Hartree-Fock Theory Using a Particle Number Projection Technique. *Phys. Rev. Lett.*, 105:192701, 2010.

[27] Sakir Ayik and Kazuyuki Sekizawa. Kinetic-energy dissipation and fluctuations in strongly damped heavy-ion collisions within the stochastic mean-field approach. *Phys. Rev. C*, 102:064619, 2020.

[28] Denis Lacroix and Sakir Ayik. Stochastic quantum dynamics beyond mean field. *Eur. Phys. J. A*, 50:95, 2014.

[29] Roger Balian and Marcel Véneroni. Time-Dependent Variational Principle for Predicting the Expectation Value of an Observable. *Phys. Rev. Lett.*, 47:1353, 1981.

[30] J. M. A. Broomfield. *Calculations of Mass Distributions using the Balian-Véneroni Variational Approach*. PhD thesis, University of Surrey, Guildford, United Kingdom, 2009.

[31] Cédric Simenel. Particle-Number Fluctuations and Correlations in Transfer Reactions Obtained Using the Balian-Vénéroni Variational Principle. *Phys. Rev. Lett.*, 106:112502, 2011.

[32] E. Williams, K. Sekizawa, D. J. Hinde, C. Simenel, M. Dasgupta, I. P. Carter, K. J. Cook, D. Y. Jeung, S. D. McNeil, C. S. Palshetkar, D. C. Rafferty, K. Ramachandran, and A. Wakhle. Exploring Zeptosecond Quantum Equilibration Dynamics: From Deep-Inelastic to Fusion-Fission Outcomes in $^{58}\mathrm{Ni} + ^{60}\mathrm{Ni}$ Reactions. *Phys. Rev. Lett.*, 120:022501, 2018.

[33] N. Edward. Derivation of the Schrödinger equation from newtonian mechanics. *Phys. Rev.*, 150:1079–1085, 1966.

[34] Denis Lacroix, Yusuke Tanimura, Sakir Ayik, and Bulent Yilmaz. A simplified BBGKY hierarchy for correlated fermions from a stochastic mean-field approach. *Eur. Phys. J. A*, 52:1–10, 2016.

[35] S. Ayik, K. Washiyama, and D. Lacroix. Fluctuation and dissipation dynamics in fusion reactions from a stochastic mean-field approach. *Phys. Rev. C*, 79:054606, 2009.

[36] Kouhei Washiyama, Sakir Ayik, and Denis Lacroix. Mass dispersion in transfer reactions with a stochastic mean-field theory. *Phys. Rev. C*, 80:031602, 2009.

[37] B. Yilmaz, S. Ayik, D. Lacroix, and K. Washiyama. Nucleon exchange mechanism in heavy-ion collisions at near-barrier energies. *Phys. Rev. C*, 83:064615, 2011.

[38] B. Yilmaz, S. Ayik, D. Lacroix, and O. Yilmaz. Nucleon exchange in heavy-ion collisions within a stochastic mean-field approach. *Phys. Rev. C*, 90:024613, 2014.

[39] S. Ayik, B. Yilmaz, and O. Yilmaz. Multinucleon exchange in quasifission reactions. *Phys. Rev. C*, 92:064615, 2015.

[40] S. Ayik, O. Yilmaz, B. Yilmaz, and A. S. Umar. Quantal nucleon diffusion: Central collisions of symmetric nuclei. *Phys. Rev. C*, 94:044624, 2016.

[41] S. Ayik, O. Yilmaz, B. Yilmaz, A. S. Umar, A. Gokalp, G. Turan, and D. Lacroix. Quantal description of nucleon exchange in a stochastic mean-field approach. *Phys. Rev. C*, 91:054601, 2015.

[42] S. Ayik, B. Yilmaz, O. Yilmaz, A. S. Umar, and G. Turan. Multinucleon transfer in central collisions of $^{238}\mathrm{U} + ^{238}\mathrm{U}$. *Phys. Rev. C*, 96:024611, 2017.

[43] S. Ayik, B. Yilmaz, O. Yilmaz, and A. S. Umar. Quantal diffusion description of multinucleon transfers in heavy–ion collisions. *Phys. Rev. C*, 97:054618, 2018.

[44] O. Yilmaz, G. Turan, and B. Yilmaz. Quasi-fission and fusion-fission reactions in $^{48}\mathrm{Ca} + ^{208}\mathrm{Pb}$ collisions at $E_{\mathrm{c.m.}} = 190$ MeV. *Eur. Phys. J. A*, 56:37, 2020.

[45] B. Yilmaz, S. Ayik, O. Yilmaz, and A. S. Umar. Multinucleon transfer in $^{58}\mathrm{Ni} + ^{60}\mathrm{Ni}$ and $^{60}\mathrm{Ni} + ^{60}\mathrm{Ni}$ in a stochastic mean-field approach. *Phys. Rev. C*, 98:034604, 2018.

[46] S. Ayik, B. Yilmaz, O. Yilmaz, and A. S. Umar. Quantal diffusion approach for multinucleon transfers in $\mathrm{Xe} + \mathrm{Pb}$ collisions. *Phys. Rev. C*, 100:014609, 2019.

[47] Kazuyuki Sekizawa and Sakir Ayik. Quantal diffusion approach for multinucleon transfer processes in the $^{58,64}\mathrm{Ni} + ^{208}\mathrm{Pb}$ reactions: Toward the production of unknown neutron-rich nuclei. *Phys. Rev. C*, 102:014620, 2020.

[48] S. Ayik, B. Yilmaz, O. Yilmaz, and A. S. Umar. Merging of transport theory with the time-dependent Hartree-Fock approach: Multinucleon transfer in $\mathrm{U}+\mathrm{U}$ collisions. *Phys. Rev. C*, 102:024619, 2020.

[49] S. Ayik, M. Arik, O. Yilmaz, B. Yilmaz, and A. S. Umar. Multinucleon transfer mechanism in $^{250}\mathrm{Cf} + ^{232}\mathrm{Th}$ collisions using the quantal transport description based on the stochastic mean-field approach. *Phys. Rev. C*, 107:014609, 2023.

[50] S. Ayik, M. Arik, E. Erbayri, O. Yilmaz, and A. S. Umar. Multinucleon transfer mechanism in $^{160}\mathrm{Gd} + ^{186}\mathrm{W}$ collisions in stochastic mean-field theory. *Phys. Rev. C*, 108:054605, 2023.

[51] S. Ayik, O. Yilmaz, B. Yilmaz, and A. S. Umar. Heavy-isotope production in $^{136}\mathrm{Xe} + ^{208}\mathrm{Pb}$ collisions at $E_{\mathrm{c.m.}} = 514$ MeV. *Phys. Rev. C*, 100:044614, 2019.

[52] M. Arik, S. Ayik, O. Yilmaz, and A. S. Umar. Description of the multinucleon transfer mechanism for $^{48}\mathrm{Ca} + ^{244}\mathrm{Pu}$ and $^{86}\mathrm{Kr} + ^{198}\mathrm{Pt}$ reactions in a quantal transport approach. *Phys. Rev. C*, 108:064604, 2023.

[53] Kayaalp, A., Ocal, S. E., Yaprakli, B., Arik, M., Ayik, S., Yilmaz, O., and Umar, A. S. A theoretical study on quasifission and fusion–fission processes in heavy-ion collisions. *Eur. Phys. J. A*, 60:79, 2024.

[54] A. Kayaalp, M. Arik, S.E. Ocal, O. Yilmaz, S. Ayik, and A.S. Umar. A quantal diffusion approach for multinucleon transfer in heavy-ion collisions. *Nuclear Physics A*, 1050:122916, 2024.

[55] Hannes Risken and Till Frank. *The Fokker–Planck Equation*. Springer–Verlag, Berlin, 1996.

[56] See Supplemental Material `http://link.aps.org/supplemental/10.1103/PhysRevC.108.064604` for an extended discussion of the calculations presented in this work.

[57] R. Charity. GEMINI: A code to simulate the decay of a compound nucleus by a series of binary decays. Technical report, International Atomic Energy Agency (IAEA), 2008. INDC(NDS)–0530.

[58] A. V. Karpov and V. V. Saiko. Modeling near-barrier collisions of heavy ions based on a Langevin-type approach. *Phys. Rev. C*, 96:024618, 2017.

[59] Itkis, M. G., Knyazheva, G. N., Itkis, I. M., and Kozulin, E. M. Experimental investigation of cross sections for the production of heavy and superheavy nuclei. *Eur. Phys. J. A*, 58:178, 2022.

[60] M. G. Itkis, E. Vardaci, I. M. Itkis, G. N. Knyazheva, and E. M. Kozulin. Fusion and fission of heavy and superheavy nuclei (experiment). *Nucl. Phys. A*, 944:204–237, 2015.

[61] Aage Winther. Grazing reactions in collisions between heavy nuclei. *Nucl. Phys. A*, 572:191–235, 1994.

[62] Aage Winther. Dissipation, polarization and fluctuation in grazing heavy-ion

collisions and the boundary to the chaotic regime. *Nucl. Phys. A*, 594:203–245, 1995.

[63] Zhi Cheng and XiaoJun Bao. Possibilities of synthesizing new proton-rich nuclei with $40 \leq Z \leq 60$ using multinucleon transfer reactions. *Chinese Phys. C*, 46:094102, 2022.

[64] D. D. Zhang, B. Li, D. Vretenar, T. Nikšić, Z. X. Ren, P. W. Zhao, and J. Meng. Ternary quasifission in collisions of actinide nuclei. *Phys. Rev. C*, 109:024316, 2024.

[65] Bulent Yilmaz, Denis Lacroix, and Resul Curebal. Importance of realistic phase-space representations of initial quantum fluctuations using the stochastic mean-field approach for fermions. *Phys. Rev. C*, 90:054617, 2014.

[66] Ibrahim Ulgen, Bulent Yilmaz, and Denis Lacroix. Impact of initial fluctuations on the dissipative dynamics of interacting Fermi systems: A model case study. *Phys. Rev. C*, 100:054603, 2019.

[67] Czuba, Thomas, Lacroix, Denis, Regnier, David, Ulgen, Ibrahim, and Yilmaz, Bulent. Combining phase-space and time-dependent reduced density matrix approach to describe the dynamics of interacting fermions. *Eur. Phys. J. A*, 56:111, 2020.